Microscopic descriptions of superdeformed bands with the Gogny force: Configuration mixing calculations in the $A\sim190$ mass region

J. Libert*
Centre d'Etudes Nucléaires de Bordeaux Gradignan, Centre National de la Recherche Scientifique-IN2P3 and Université Bordeaux-I, Bôite Postale 120, F-33175 Gradignan Cedex, France

M. Girod and J.-P. Delaroche
Commissariat à l'Energie Atomique, Service de Physique Nucléaire, Bôite Postale 12, F-91680 Bruyères-le-Châtel, France
(Received 26 March 1999; published 27 September 1999)

A quantal Hamiltonian $\hat{\mathcal{H}}_{\rm coll}$ expressed in terms of the five collective quadrupole coordinates is built for eight nuclei (^{190,192,194}Hg, ^{192,194,196}Pb, and ^{196,198}Po) which display secondary minima at large elongation in their potential energy surface. These surfaces as well as the tensor of inertia entering $\hat{\mathcal{H}}_{\rm coll}$ are deduced from constrained Hartree-Fock-Bogoliubov calculations based on Gogny force. A two-center basis method employed to solve $\hat{\mathcal{H}}_{\rm coll}$ is presented. The stability of predicted collective spectra is discussed. Yrast and vibrational $\pi=+$ superdeformed (SD) bands are predicted together with collective bands at normal deformation (ND). The predicted yrast SD bands at low spin display properties which compare favorably with experimental information. Quite good agreement is in particular obtained for the isomeric energies of nuclei for which the link between SD and ND levels is experimentally known. Among the excited SD bands which are here predicted, those built on top of β vibrations are lower in energy. Only for the ^{196,198}Po isotopes are these excitation energies falling in the low energy range $E\sim0.8$–1.0 MeV. These properties should favor an experimental discovery of β-vibrational SD bands in the $A\sim190$ mass region. [S0556-2813(99)03709-7]

PACS number(s): 21.60.Jz, 21.60.Ev, 21.10.Re, 27.80.+w

I. INTRODUCTION

The discovery of fission isomers [1] in the early 1960s has opened a broad field of experimental and theoretical studies focusing on the structure properties of nuclei at large elongation. Shell effects stand at the origin of these phenomena, as shown by Strutinsky using the celebrated shell correction method [2]. Since that time, the Strutinsky method has been used in various related topics, among which are shape isomerism in medium and heavy nuclei [3–6], and shape coexistence and transition [7,8].

A major success of the shell correction method implemented within the Cranking model has been the prediction and interpretation of superdeformation (SD) phenomena in fast rotating nuclei [9–17]. Since the discovery of SD states at high spins in ^{152}Dy [18], many yrast and excited SD bands have been observed, not only in the $A\sim150$ mass region but also for $A\sim60$, 80, 130, 140, and 190 [19]. These measurements reveal many facets of SD nuclear properties at high rotational frequencies, which are reviewed in Refs. [20–24].

This database also serves as valuable information for challenging self-consistent mean field predictions, among which are quadrupole moments, moments of inertia, and collective as well as quasiparticle (qp) excitations at superdeformed shapes. In this respect, the $A\sim190$ region is of special interest since SD states have been observed down to quite low spin (for instance $I=6$ for the yrast SD band of ^{194}Pb [25]). That $I=0$ shape isomers have so far escaped observation in this mass region is probably related to the specific character of the fusion-evaporation method employed in such experiments. However, nonrotating SD states should exist in the $A\sim190$ region because the strong shell effect at major-to-minor axis ratio $a:b\sim1.7$ is always predicted by self-consistent (and phenomenological) mean field approaches, whether or not the SD shapes are rotating.

Various self-consistent mean-field approaches have been used for describing and predicting SD state properties. These approaches form two distinct families. The first one includes the constrained HF+BCS and HFB methods implemented with Skyrme [26–30] or Gogny force [31–33], as well as the relativistic mean field (RMF) theory [34,35]. Calculations based on these approaches provide potential energy surfaces from which excitation energies of nonrotating SD states are estimated [6,36–41]. More complete predictions for both yrast nonrotating states and phonon excitations at SD shapes in the $A\sim190$ region are obtained in the context of the generator coordinate method (GCM). This method has been applied to the case where one collective coordinate is considered [42]. The GCM problem for two collective coordinates has also been solved for octupole modes [43]. Moreover, a two dimensions GCM approach for quadrupole modes has been applied to superdeformation at no spin in the actinides [44]. This model may be extended to include rotation using the Gaussian overlap approximation (GOA). Results of GCM+GOA calculations for the five collective quadrupole coordinates are published in Ref. [45] for normal deformed nuclei and in [46,47] for SD properties of mercury isotopes. The second family includes all the HFB cranking approaches which treat self-consistently rotational motion but ignore

*Present address: Commissariat à l'Energie Atomique, Service de Physique Nucléaire, Bôite Postale 12, F-91680 Bruyères-le-Châtel, France.

coupling to other collective modes of excitation. Self-consistent cranking calculations have been performed in the $A\sim 190$ SD region using Skyrme forces complemented with various treatments of the pairing field [48–50], as well as with Gogny force [51–53]. Cranked RMF calculations have also been carried out in the $A\sim 150$ SD region [54].

Our GCM+GOA calculations [46,47,52] based on the finite range, density dependent D1S Gogny force [31–33] have been extended to cover even-even nuclei of the $A=190-200$ region and predict systematic properties of their yrast and collective quadrupole SD bands. To render this study as complete as possible, here we also present a detailed account of the microscopic ingredients and original methods used to produce our predictions. Furthermore, these systematic predictions now cover the spin range $I=0-22$ for all nuclei but ^{194}Pb for which this range is extended to $I_{\max}=30$. New numerical methods as well as moments of inertia now determined with a level of approximation superior to that conveyed by the Inglis-Belyaev formula [55,56] are employed, which leads to an improvement over our previous predictions [46,47]. First, a linear relationship between elongation coordinate β and mass quadrupole moments is imposed. This brings in no new physics, but leads to a scale for β which significantly differs from that shown for example in Fig. 1 of Ref. [46]. With this new definition, the SD potential minima of Hg isotopes get shifted for $\beta\sim 0.55$ to the present value $\beta\sim 0.65$ (see text). The main advantage of adopting the above-mentioned linear relationship is to release the small deformation approximation employed previously in the calculation of vibrational collective masses. As a result, the relative excitation energies of predicted SD bands get lowered at most by a few hundred of keV. Finally, significant improvements in our collective model are obtained through scaling the Inglis-Belyaev moments of inertia to those calculated in the manner of Thouless-Valatin [57], as explained in the main text. For all these reasons, the present calculations are brand new. They deal not only with the ^{190,192,194}Hg but also with the ^{192,194,196}Pb and ^{196,198}Po isotopes.

The present work is organized as follows. In Sec. II, a presentation of our configuration mixing method is offered. It includes a discussion on the collective masses, moments of inertia, zero-point energies and overlap kernels used as inputs to a collective Hamiltonian $\hat{\mathcal{H}}_{\rm coll}$ in five dimensions. In Sec. III (and the Appendix), we present a two-center basis method to solve $\hat{\mathcal{H}}_{\rm coll}$, discuss the numerical stability of eigenstates predicted for spins up to $I=30$, and explain how $E2$ reduced transition probabilities are calculated for intra- and inter-SD band transitions. Section IV is devoted to the single particle, pairing, and potential properties in the vicinity of SD potential minima. Section V includes an analysis of the SD level geometric properties, which leads to the identification in our spectra of yrast and one-quadrupole-phonon, β and γ SD bands. Finally, the predicted excitation energies, transition quadrupole moments, and kinematic moments of inertia for yrast SD bands are compared with available measurements in Sec. VI. Here are also discussed dynamical properties of the β and γ SD bands, and implications of our predictions regarding whether or not these excited bands might be observed. Large scale cranked HFB calculations have also been performed to high rotational frequency for kinematic and dynamic moments of inertia relevant to the Hg, Pb, and Po SD nuclei. These results will be presented in a forthcoming paper.

II. CONFIGURATION MIXING METHOD

The GCM method has been used extensively to treat various aspects of dynamical phenomena ever since the pioneering work of Griffin, Hill, and Wheeler [58]. This method complemented with the GOA assumption is subject to detailed discussions in [59]. Here, we only give the main steps to establish our notations.

A. Building a collective Hamiltonian $\hat{\mathcal{H}}_{\rm coll}$ in five dimensions

The correlated states $|\Psi_i\rangle$ (i.e., the ground state as well as excited states) of a nucleus are sought as

$$|\Psi_i\rangle=\int f_i(q)|\Phi_q\rangle dq, \tag{1}$$

where $|\Phi_q\rangle$ is the quasiparticle (qp) vacuum of the many-body nuclear Hamiltonian $\hat{H},q$ a set of collective coordinates, and $f_i(q)$ the superposition amplitude for the ith eigenstate. This amplitude is solution of the Griffin, Hill, and Wheeler equation

$$\int [H(q,q')-E_iN(q,q')]f_i(q')dq'=0, \tag{2}$$

in which $N(q,q')=\langle\Phi_q|\Phi_{q'}\rangle$ is the overlap kernel, $H(q,q')=\langle\Phi_q|\hat{H}|\Phi_{q'}\rangle$ the Hamiltonian kernel, and E_i the expectation value

$$E_i=\frac{\langle\Psi_i|\hat{H}|\Psi_i\rangle}{\langle\Psi_i|\Psi_i\rangle}. \tag{3}$$

Solving Eq. (2) has been accomplished recently in one dimension ($q_0=r^2Y_{20}$) and two dimensions ($(q_0=r^2Y_{20},\ q_3=r^3Y_{30})$ and $[q_0=r^2Y_{20},\ q_2=r^2(Y_{22}+Y_{2-2})]$) using Skyrme forces [42,44]. In the present work, our aim is to treat the q_0, q_2 and rotational degrees of freedom. We therefore have to deal with the five quadrupole collective coordinates. In this context, solving Eq. (2) is a formidable task which has been alleviated by using the Gaussian overlap approximation. In the GCM+GOA method [60–62], it is assumed that the overlap kernel $N(q,q')$ is a Gaussian shape. A second order expansion over the nonlocality in the coordinates $(q-q')$ leads to transforming Eq. (2) into a second order differential equation which has the character of a collective Hamiltonian $\hat{\mathcal{H}}_{\rm coll}$. The eigenvalue problem to solve now reads

$$\hat{\mathcal{H}}_{\rm coll}g_i(q)=E_ig_i(q), \tag{4}$$

where

$$g(q)=\int [N(q,q')]^{1/2} f(q')dq' \tag{5}$$

and

$$\hat{\mathcal{H}}_{\rm coll}=-\frac{\hbar^2}{2}\sum_{i,j}\frac{\partial}{\partial q_i}[M^{-1}(q)]_{ij}\frac{\partial}{\partial q_j}+\mathcal{V}(q). \tag{6}$$

In Eq. (6), $\mathcal{V}(q)$ is the potential energy surface (PES)

$$\mathcal{V}(q)=V(q)-\Delta V(q), \tag{7}$$

where

$$V(q)=H(q,q), \tag{8}$$

and where $\Delta V(q)$ is the zero point energy (ZPE) stemming from the expansion of $H(q,q')$ over nonlocality. Furthermore, $M_{i,j}(q)$ is the tensor of inertia.

Going a step further, we reexpress $\hat{\mathcal{H}}_{\rm coll}$ in terms of the intrinsic quadrupole coordinates q_0 and q_2, and Euler angles $\Omega=(\theta_1,\theta_2,\theta_3)$. Assuming a local approximation in these angular coordinates, the tensor M_{ij} now can be defined through its components: (i) the collective masses $B_{ij}(q_0,q_2)$ with $(i,j)=(0\ and\ 2)$ and (ii) the moments of inertia $\mathcal{J}_k(q_0,q_2)$ where k refers to the principal axes ($k=1$, 2, and 3). In this context, the physical content of $\hat{\mathcal{H}}_{\rm coll}$ is clear: $\hat{\mathcal{H}}_{\rm coll}$ describes rotation, quadrupole vibrations, and coupling between these collective modes. This Hamiltonian is quantal in nature. Its structure is formally identical to that considered years ago by Kumar and Baranger [63].

For the kinetic energy term, the expansion over nonlocality leads to mass parameters which we call GCM+GOA masses. Whether or not to use these masses in $\hat{\mathcal{H}}_{\rm coll}$, known to be systematically too weak, has been for years a controversial debate running among the community [62,64–66]. This issue is related to that Eq. (1) is too restrictive a definition of physical states, which therefore should also be extended to include p, the conjugate coordinate of q, as suggested in particular by Villars [65]. We did not perform this extension. Instead, we have adopted the view [59] that the collective Hamiltonian (6) is formally identical to a quantized adiabatic time dependent Hartree-Fock-Bogoliubov (ATDHFB) Hamiltonian. This semiclassical approach which preserves the formal symmetry between the collective coordinate q and its conjugate p, is known to produce the exact mass parameter in the particular case of translation.

Here, the ATDHFB theory is employed in its perturbative limit, i.e., the so-called Cranking approximation, to calculate the tensor of inertia. However, for the rotational degrees of freedom, the perturbative expression for the moment inertia, known as the Inglis-Belyaev cranking formula [55,56], has been corrected to include in an approximate way the Thouless-Valatin (TV) dynamical rearrangement [57]. The TV moments of inertia are calculated in the fully self-consistent dynamical (i.e., cranked HFB) approach to the rotational motion in the vicinity of spin zero. Furthermore, the treatment of vibrational mass parameters is restricted to the Cranking expressions stemming from the standard linear response theory [59]. Finally, consistent perturbative expressions are naturally used to evaluate the ZPE terms in the potential. The explicit forms of the Cranking series for the vibrational kinetic energy and the ZPE terms are given in Secs. II B 4 and II B 5.

B. Potential and tensor of inertia

The tensor of inertia and potential entering $\hat{\mathcal{H}}_{coll}$ are calculated using the constrained Hartree-Fock-Bogoliubov (CHFB) method.

1. Constrained HFB method

The CHFB method consists in applying the variational principle to the energy functional obtained for the qp vacuum Φ_q, i.e.,

$$\delta\langle\Phi_q|\hat{H}-\lambda_0\hat{Q}_0-\lambda_2\hat{Q}_2-\lambda_Z\hat{Z}-\lambda_N\hat{N}|\Phi_q\rangle=0. \tag{9}$$

In this equation, (i) $\hat{H}$ is the nuclear Hamiltonian in which the potential component is defined using the D1S Gogny effective force [31–33], (ii) $\hat{Q}_0$ and $\hat{Q}_2$ are external field operators generating axial and triaxial quadrupole deformations, respectively, and (iii) $\hat{Z}$ and $\hat{N}$ are the proton and neutron numbers operators, respectively. The Lagrange multipliers $\{\lambda_i\}$ are determined from the constraints

$$\langle\Phi_q|\hat{N}|\Phi_q\rangle=N,\quad \langle\Phi_q|\hat{Z}|\Phi_q\rangle=Z,\quad \langle\Phi_q|\hat{Q}_i|\Phi_q\rangle=q_i\,. \tag{10}$$

The system of equations (9), (10) is numerically solved at each deformation q_i by expanding the single particle states into triaxial harmonic oscillator bases as explained in Ref. [67]. Here, the adopted bases include twelve major shells.

2. Deformation energy surface

Once the constrained HFB problem has been solved, the deformation energy surface $V(q)$ entering Eq. (7) is calculated as

$$V(q)=\langle\Phi_q|\hat{H}|\Phi_q\rangle, \tag{11}$$

where q stands for the set (q_0,q_2). The quadrupole coordinates q_0 and q_2 are directly related to the polar Bohr deformations β and γ through the relations

$$\beta=\sqrt{\frac{\pi}{5}}\frac{\sqrt{q_0^2+3q_2^2}}{A\langle r^2\rangle} \tag{12}$$

and

$$\gamma=\arctan\sqrt{3}\,\frac{q_2}{q_0}. \tag{13}$$

Cartesian coordinates are also employed in our work; they are defined as

$$a_0=\beta\cos\gamma,\quad a_2=\beta\sin\gamma. \tag{14}$$

A and $\langle r^2 \rangle$ are the nuclear mass and mean square radius of the mass distribution, respectively. To make β linearly dependent upon quadrupole moment, $\langle r^2 \rangle$ has not been evaluated explicitly in Eq. (12). In contrast with our earlier works [46,47], here we adopt the liquid drop model estimate

$$\langle r^2 \rangle_{\rm LD} = \frac{3}{5}(r_0 A^{1/3})^2, \tag{15}$$

with $r_0 = 1.2$ fm. With this definition, β gets stretched as compared with the earlier values in Refs. [46,47] and now transforms into a scaled mass quadrupole moment. Furthermore, the energy surfaces (7) and (11) may be expressed in terms of the coordinates (12)–(14) as either $\mathcal{V}(\beta,\gamma)$ $[V(\beta,\gamma)]$ or $\mathcal{V}(a_0,a_2)$ $[V(a_0,a_2)]$.

3. Moments of inertia

For nuclei rotating around the k axis, the moment of inertia may be obtained from solving the cranked HFB equation

$$\delta \langle \phi_q^\omega | \ \hat{H} - \lambda_Z \hat{Z} - \lambda_N \hat{N} - \omega \hat{I}_k | \phi_q^\omega \rangle = 0, \tag{16}$$

where $\hat{I}_k$ is the k component of the angular momentum operator and ω the angular velocity. Introducing the notation $\langle \hat{I}_k \rangle_\omega = \langle \phi_q^\omega | \hat{I}_k | \phi_q^\omega \rangle$, the moment of inertia is obtained as

$$\mathcal{J}_k^{\rm TV} = \lim_{\omega \to 0} \frac{\langle \hat{I}_k \rangle_\omega}{\omega}. \tag{17}$$

The label TV in Eq. (17) is intended to mean that the moment of inertia contains the so-called Thouless-Valatin dynamical rearrangement contributions [57]. These contributions are neglected if a perturbative solution of Eq. (16) is sought. In this approximation, the moment of inertia then reduces to the standard Inglis-Belyaev (IB) expression [55,56]

$$\mathcal{J}_k^{\rm IB} = 2\hbar^2 \sum_{\mu\nu} \frac{|\langle \mu\nu | \hat{I}_k | \Phi \rangle|^2}{(E_\mu + E_\nu)}, \tag{18}$$

where μ and ν are quasiparticle (qp) states created on the *static* quasiparticle vacuum $\Phi = \phi^{\omega=0}$, and where E_μ and E_ν are qp energies.

As is well known [57], the IB definition (18) leads to $\mathcal{J}_k^{IB}$ values which are too small. On the other hand, solving Eq. (16) at low ω on a lattice covering the whole deformation space represents a considerable numerical task which is out of the scope of the present work. We have therefore resorted to an approximate evaluation of the $\mathcal{J}_k^{\rm TV}$ moments of inertia by scaling the $\mathcal{J}_k^{\rm IB}$ values calculated all over the $(\beta,\ \gamma)$ plane, namely, assuming

$$\mathcal{J}_k = \mathcal{J}_k^{\rm IB}(1+\alpha), \tag{19}$$

where α is a constant number estimated as follows. First, we calculate the moment of inertia defined through Eqs. (17) and (18) at a few values in the deformation space and form the ratio $R_k(q) = \mathcal{J}_k^{\rm TV}(q)/\mathcal{J}_k^{\rm IB}(q)$. An illustration is shown for ^{194}Pb in Fig. 1 where $\mathcal{J}_X^{\rm IB}$ (solid curve), $\mathcal{J}_X^{\rm TV}$ (dotted curve), and R_X (dot-dashed curve) are calculated as functions of the axial deformation β. These calculations cover deformation values from $\beta = 0.26$ to $\beta = 1.05$ where the deformation energy $V(\beta)$ [see curve labeled $E_{\rm HFB}$ in Fig. 1(a)] shows an extremum (fission barrier). As can be seen, the moments of inertia take on increasing values with growing deformation, except near the β values for which the energy $E_{\rm HFB}$ displays secondary minima (i.e., the superdeformed and hyperdeformed minima). These shoulders observed in the $\mathcal{J}_X$'s are directly related to minima in the neutron or proton pairing energy. The ratio R_X varies slowly with increasing deformation. Its values [scale shown at the right-hand side of Fig. 1(b)] are in the range 1.34–1.46 and reach a minimum $R_X = 1.34$ at superdeformation. These results show that the dynamical Thouless-Valatin correction to the perturbative expression $\mathcal{J}_X^{\rm IB}$ remains almost independent of deformation and does not introduce significant new structures in the behavior of the moments of inertia. The same calculation has

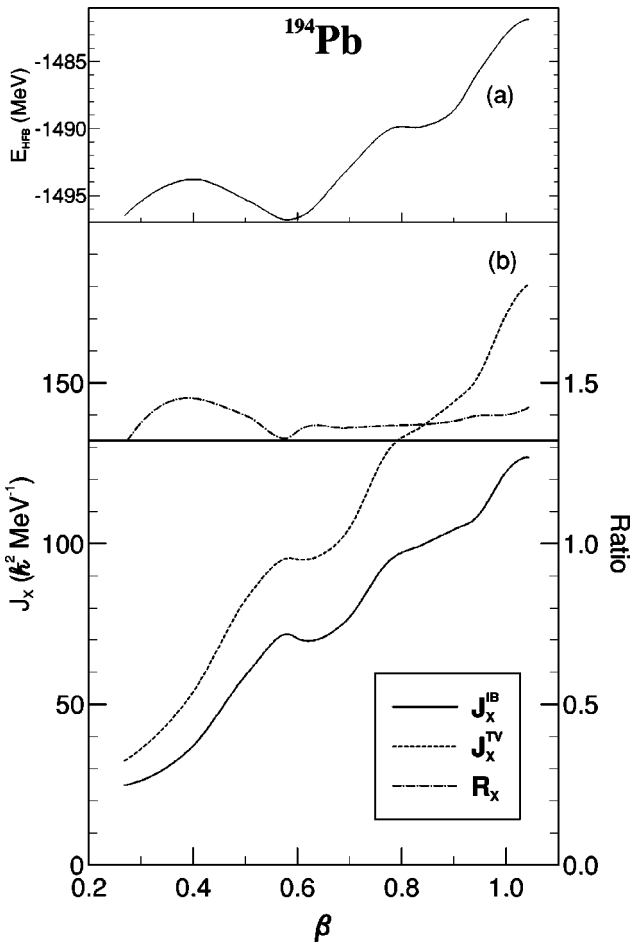

FIG. 1. ^{194}Pb isotope. (a) HFB energy (MeV) as a function of axial deformation β; (b) moments of inertia $\mathcal{J}_X^{IB}$ (solid curve) and $\mathcal{J}_X^{TV}$ (dotted curve), and ratio $R_X = \mathcal{J}_X^{IB}/\mathcal{J}_X^{TV}$ (dashed-dotted curve) as functions of β. The left-hand side scale is for moments of inertia and that for the ratio is shown as the right-hand side of the figure. The value $R_X = 1.32$ is marked by the solid line.

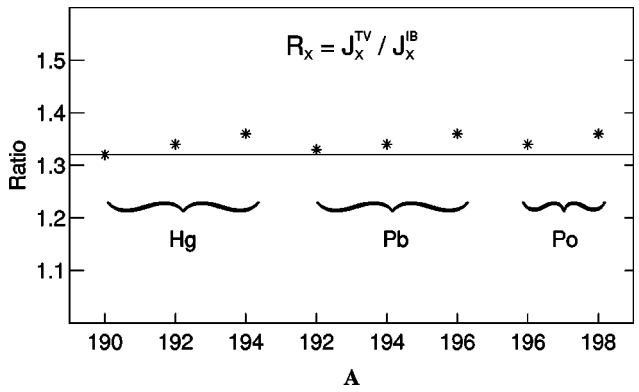

FIG. 2. R_x ratio values (asterisks) calculated at SD potential minima for the ^{190,192,194}Hg, ^{192,194,196}Pb, and ^{196,198}Po isotopes. The solid line $R_x = 1.32$ has the same meaning as in Fig. 1.

been repeated for the other nuclei of present interest. The results shown in Fig. 2 (crosses) indicate that R_X is nearly constant at superdeformed shapes through the $A=190-198$ region. On the basis of these studies, the moments of inertia $\mathcal{J}_k(q)$ entering the collective Hamiltonian (6) are calculated with the minimal prescription

$$\mathcal{J}_k(q)=(1.00+0.32)\mathcal{J}_k^{\mathrm{IB}}(q). \tag{20}$$

4. Collective masses

For a vibrational degree of freedom associated with a collective variable of generic name $q=\langle\hat{Q}\rangle$ and collective velocity $\dot{q}$., the ATDHFB equation to solve writes

$$\delta\langle\phi_q^{\dot{q}}|\ \hat{H}-\lambda_Z\hat{Z}-\lambda_N\hat{N}-\lambda\hat{Q}-\dot{q}\hat{P}|\phi_q^{\dot{q}}\rangle=0. \tag{21}$$

Assuming an adiabatic path made up with the static states $\Phi_q\equiv\phi_q^{\dot{q}=0}$ [associated with the generalized density matrix $\mathcal{R}_{\dot{q}=0}(q)$ hence from now labeled as $\mathcal{R}_0(q)$], the dynamical constraint $\hat{P}$ is defined at each deformation q through a direct generalization of the Baranger Vénéroni [64] impulsion operator

$$\hat{P}=i\hbar\left[\frac{\partial\mathcal{R}_0}{\partial q},\mathcal{R}_0\right]. \tag{22}$$

In this framework, $\langle P\rangle_{\dot{q}}=\frac{1}{2}\,\mathrm{Tr}\,\mathcal{R}_{\dot{q}}\hat{P}$ is the classical impulsion from which the mass parameter $B^{\mathrm{TV}}(q)$ is deduced

$$B^{\mathrm{TV}}(q)=\lim_{\dot{q}\to 0}\frac{\langle P\rangle_{\dot{q}}}{\dot{q}}.$$

Solving Eq. (21) is a task which is in progress [68]. Here, we have resorted to calculations based on the cranking approximation. In this context, the parameters $B_{ij}(q)$ associated with the quadrupole collective coordinates q_i and q_j with $(i,j)=(0$ and $2)$, write [59]

$$B_{ij}(q)=\frac{\hbar^2}{2}\frac{\mathcal{M}_{-3}^{ij}(q)}{[\mathcal{M}_{-1}^{ij}(q)]^2}, \tag{23}$$

where

$$\mathcal{M}_k^{ij}(q)=\sum_{\mu\nu}(E_\mu+E_\nu)^k|\overline{q_i^{\mu\nu}}\overline{q_j^{\mu\nu}}| \tag{24}$$

and

$$\overline{q_i^{\mu\nu}}=\langle\Phi_q|\,\eta_\mu\eta_\nu\hat{Q}_i|\Phi_q\rangle, \tag{25}$$

with η as a quasiparticle destruction operator. In Eq. (25), the quadrupole operators $\hat{Q}_i$ are defined as

$$\hat{Q}_0=2z^2-x^2-y^2, \tag{26}$$

and

$$\hat{Q}_2=x^2-y^2, \tag{27}$$

and the summation (24) runs over the proton and neutron qp states μ and ν.

To appreciate the range of validity of Eq. (23), it is worth mentioning that the cranking approximation to the mass parameters relies upon two simplifying assumptions, namely, (i) the variation $\partial\mathcal{R}_0/\partial q$ of the generalized density matrix along the adiabatic path is treated in a linear response approximation and (ii) the impulsion operator (22) thus obtained is used to solve Eq. (21) up to first order in $\dot{q}$, neglecting the rearrangement (i.e., Thouless-Valatin) terms of the mean field (see, e.g., Ref. [69]). The former simplifying assumption has recently been tested and found rather reliable for axial vibrations of normal and superdeformed shapes in the $A\sim 190$ region [68,70]. However, this would only be a fair statement if we were to calculate transition rates between ND and SD levels, which critically depend upon the tails of initial and final state wave functions. No detailed check of the latter assumption exists so far. However, previous studies in which Skyrme forces are used without [71] and with pairing field included [72] indicate that the Thouless-Valatin corrections (i) weakly depend upon deformation and (ii) should increase the mass parameters by no more than 10%. Sensitivity calculations here performed for ^{194}Pb show that increasing the vibrational mass parameters (23) by 10% lowers the absolute ground state energy by 120 keV and decreases the relative excitation energy of the first two SD bands by 15 and 18 keV, respectively. This small alteration of the predicted SD vibrational energy spectra suggests that the cranking approximation (23) is reasonable for calculating the mass parameters.

5. Overlap kernel and zero point energy

Within the GOA approximation, the actual overlap kernel [see Eq. (2)] for any of the collective variables q_i writes

$$N(q_i,q_j')=\exp\left[-\frac{1}{2}G_{ij}(q)(q_i-q_j')^2\right], \tag{28}$$

where $G_{i,j}(q)$ presumably displays a slow dependence upon q. Following Ref. [59], the Gaussian width $\sigma^{ij}(q)$ is

$$G_{ij}(q)=\frac{1}{\sigma^{ij}(q)^2}=\frac{\mathcal{M}^{ij}_{-2}(q)}{\mathcal{M}^{ij}_{-1}(q)^2}, \tag{29}$$

where the moments $\mathcal{M}^{ij}_k$ are calculated according to Eq. (24). Once $G_{i,j}(q)$ and $N(q_i,q'_j)$ are obtained, the superposition amplitude $f(q)$ is deduced from Eq. (5) through an inverse Gauss transform, and used to calculate electromagnetic transition rates (see Sec. III C).

The zero point energy $\Delta V(q)$ includes terms originating from the kinetic energies (i.e., rotation and vibrations) and potential energy. It reads

$$\Delta V(q)=\Delta V_{\rm vib}(q)+\Delta V_{\rm rot}(q)+\Delta V_{\rm pot}(q). \tag{30}$$

Since we have checked that the term $\Delta V_{\rm pot}(q)$ is small as compared with the other two ΔV components, $\Delta V_{\rm pot}(q)$ is ignored throughout our study. The vibrational component $\Delta V_{\rm vib}(q)$, calculated at the same level of approximation as that for the masses B_{ij}, writes [59]

$$\Delta V_{\rm vib}(q)=\sum_{i,j=0,2}\Delta V_{ij}(q), \tag{31}$$

with

$$\Delta V_{ij}(q)=\frac{\mathcal{M}^{ij}_{-2}(q)}{\mathcal{M}^{ij}_{-3}(q)}. \tag{32}$$

Finally, the rotational term $\Delta V_{\rm rot}(q)$ is made up with three pieces

$$\Delta V_{\rm rot}(q)=\Delta V_{-2-2}(q)+\Delta V_{-1-1}(q)+\Delta V_{11}(q). \tag{33}$$

Each term is calculated [59] using the moments $\mathcal{M}^{ij}_k$ (24) in which the intrinsic components of the quadrupole operator are

$$\hat{Q}_1=-2iyz,\quad \hat{Q}_{-1}=-2xz,\quad \hat{Q}_{-2}=2ixy. \tag{34}$$

The potential energy $\mathcal{V}$ (7) and components (31) and (33) of ΔV (30) calculated for ^{194}Hg are shown in Figs. 3(a) and 3(b) as functions of axial deformation. As can be seen, ΔV is dominated by its $\Delta V_{\rm rot}$ component (dashed curve) which increases with increasing β. The net effect of considering ΔV (30) is to make deeper the SD potential landscape and to lower its minimum by 1 to 1.7 MeV depending upon the nucleus under consideration. All the potential energy surfaces used for solving $\hat{\mathcal{H}}_{\rm coll}$ include the ZPE contributions.

III. SOLVING $\hat{\mathcal{H}}_{\rm coll}$

A. Expansion of eigenstates on a basis

The collective masses B_{ij} (23), moments of inertia $\mathcal{J}_k$ (20), and potential $\mathcal{V}$ (7) serve to define $\hat{\mathcal{H}}_{\rm coll}$ (6). When expressed in terms of the coordinates a_0 and a_2 (14) and Euler angles $\Omega=(\theta_1,\theta_2,\theta_3)$, it has the Bohr Hamiltonian form [73]

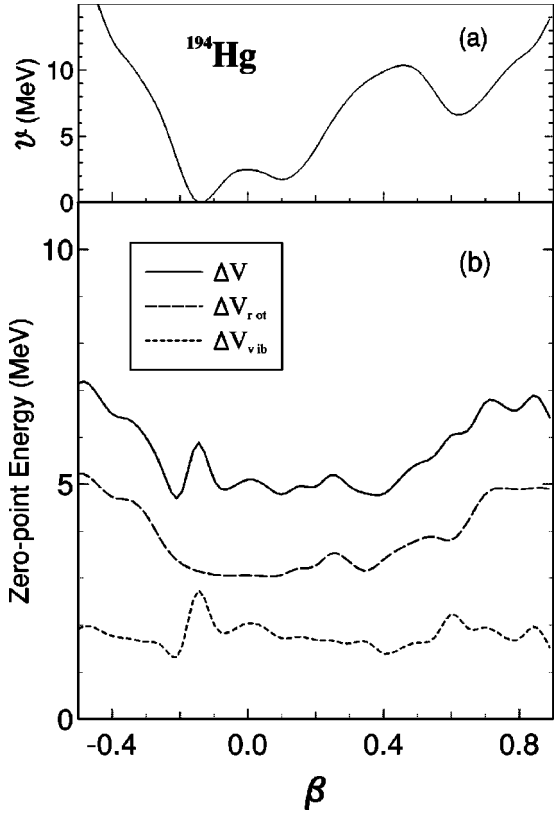

FIG. 3. ^{194}Hg isotope. (a) HFB energy (labeled $\mathcal{V}$) as a function of axial deformation. The values are shifted so that $\mathcal{V}=0$ at the normal deformed minimum; (b) Zero point energies: $\Delta V_{\rm rot}$ (dashed curve), $\Delta V_{\rm vib}$ (dotted curve), and $\Delta V=\Delta V_{\rm vib}+\Delta V_{\rm rot}$ (solid curve).

$$\hat{\mathcal{H}}_{\rm coll}=\frac{1}{2}\sum_{k=1}^{3}\frac{\hat{I}_k^2}{\mathcal{J}_k}-\frac{1}{2}\sum_{m,n=0\ \text{and}\ 2}D^{-1/2}\frac{\partial}{\partial a_m}D^{1/2}G^{mn}\frac{\partial}{\partial a_n}+\mathcal{V}. \tag{35}$$

In this expression, $\hat{I}_k$ is the k component of angular momentum I in the intrinsic system acting on the Euler angles portion of the collective space, and

$$D=(B_{00}B_{22}-B_{02}^2)\prod_k\mathcal{J}_k \tag{36}$$

is the metric. Furthermore, G^{mn} is the matrix

$$G^{mn}=(B_{mn})^{-1}, \tag{37}$$

where B_{mn} is a collective mass (23). Since the mass B_{mn} and inertia $\mathcal{J}_k$ parameters as well as the potential $\mathcal{V}$ which all depend upon the deformation variables (a_0,a_2) are deduced numerically from HFB wave functions (see Sec. II), $\hat{\mathcal{H}}_{\rm coll}$ possesses no analytical solutions. The eigenstates $|\Psi_i\rangle$ fulfilling the norm condition

$$\langle\Psi_i|\Psi_j\rangle=\int d\Omega\int\Psi_i^*\Psi_jD^{1/2}da_0da_2=\delta_{ij}, \tag{38}$$

and the eigenenergies E_i are obtained as numerical solutions of the equation

$$\hat{\mathcal{H}}_{\rm coll}|\Psi_i\rangle = E_i|\Psi_i\rangle. \tag{39}$$

These solutions are sought for through expanding the $|\Psi_i\rangle$'s onto an orthonormalized set of two-center basis functions as explained in the Appendix. Briefly, the solutions of Eq. (39) may be expressed in the (a_0,a_2) coordinates as

$$\Psi_{IM\alpha} = \sum_{j=1}^{N_I} C_j^{I\alpha} \psi_j^{IM}(a_0,a_2,\Omega), \tag{40}$$

where

$$\psi_j^{IM}(a_0,a_2,\Omega) = \sum_K{}' \; A_j^{IK}(a_0,a_2)\varphi_{MK}^I(\Omega) \tag{41}$$

is the jth vector of the orthonormalized basis in the subspace of angular momentum I, and where the symbol Σ_K' means that the summation over K is limited to the even positive K values, with $K\neq 0$ for odd I. Furthermore, (i) $\varphi_{MK}^I(\Omega)$ is the standard, normalized linear combination of Wigner rotation matrices $\mathcal{D}_{MK}^I(\Omega)$ and $\mathcal{D}_{M-K}^I(\Omega)$ (see the Appendix), (ii) $A_j^{IK}(a_0,a_2)$ is a vibrational amplitude, (iii) α is a label to distinguish between eigenstates in the block of spin I, (iv) $C_j^{I\alpha}$ is an expansion coefficient, and (v) N_I the dimension of the subspace of angular momentum I considered in actual calculations.

B. Stability of collective energy spectra

A detailed presentation of the numerical method employed for solving Eq. (39) is given in the Appendix.

Since $\hat{\mathcal{H}}_{\rm coll}$ is solved on a finite size basis, it is mandatory to check the stability of our predictions. This is performed by increasing step by step the basis size for each spin block. The basis size N_I is directly related to the order $m_{\rm max}$ in the power expansion of vibrational amplitudes in terms of the coordinates a_0 and a_2. Our numerical results are illustrated for ^{192}Hg in Fig. 4 where $m_{\rm max}$ is gradually increased, from $m_{\rm max}=20$ to $m_{\rm max}=36$, separately for the spin blocks $I=0$, 10, and 20. In this range of $m_{\rm max}$ values, the number N_I (labeled $N_I^{\rm ortho}$ in the figure) of independent basis states in each spin block roughly increases by a factor of 2. The various lines represent the differences in energy

$$\Delta E_{I\alpha,m_{\rm max}} = E_{I\alpha,m_{\rm max}} - E_{I\alpha,20} \tag{42}$$

calculated for the first levels in a given spin block. As can be seen, the differences $\Delta E_{I\alpha,36}$ and $\Delta E_{I\alpha,34}$ never exceed 5 keV, which suggests that the absolute energies predicted for each level are obtained with an accuracy better than 10 keV. Similar accuracies are also obtained when solving $\hat{\mathcal{H}}_{\rm coll}$ for the other nuclei of present interest. The least stable solutions are for eigenstates which are neither purely superdeformed nor normal deformed. All the predictions shown and discussed later on are based on calculations in which $m_{\rm max}=36$ is used.

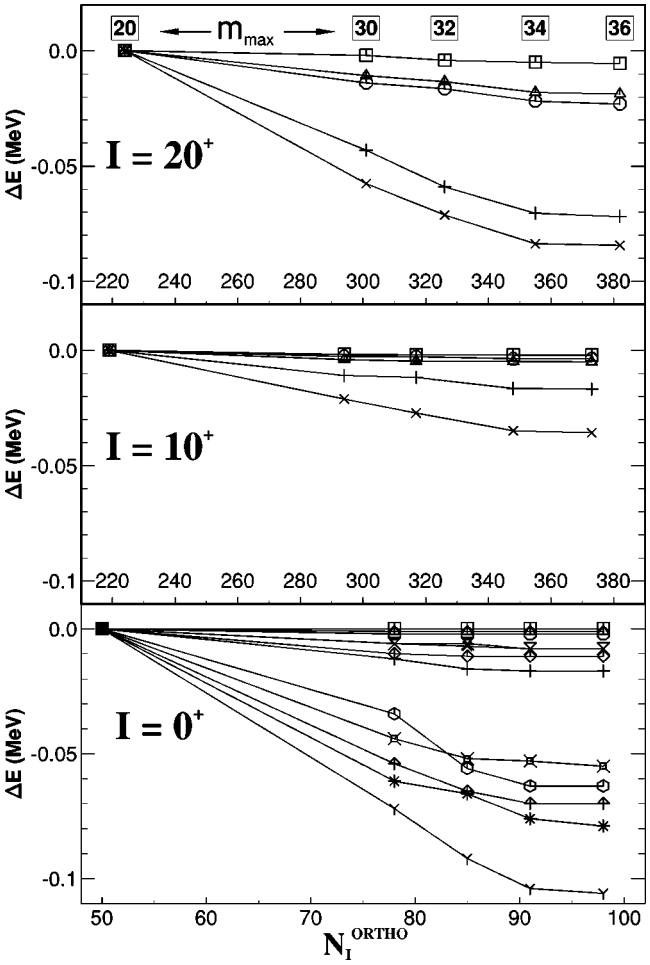

FIG. 4. ^{192}Hg isotope. Differences in energy $\Delta E_{I\alpha,m_{\rm max}} = E_{I\alpha,m_{\rm max}} - E_{I\alpha,20}$ [see Eq. (42)] calculated for the first collective levels (symbols connected with solid lines) predicted in the spin blocks $I^\pi = 0^+$ (bottom), 10^+ (middle), and 20^+ (top), as functions of $m_{\rm max}$ and $N_{I=0}^{\rm ORTHO}$, $N_{I=10}^{\rm ORTHO}$ and $N_{I=20}^{\rm ORTHO}$, respectively.

C. $E2$ reduced transition probabilities

The correlated wave functions (1) in five dimensions read

$$|IM\alpha\rangle = \sum_K{}' \int f_{IK\alpha}(a_0,a_2)\varphi_{MK}^I(\Omega)R(\Omega)\Phi_{a_0,a_2} \times D^{1/2} da_0 da_2 d\Omega,$$

where $f_{IK\alpha}$ is the K component of the superposition amplitude deduced from the inverse Gauss transform of Eq. (40) as explained below, $R(\Omega)$ the rotation operator, and Φ_{a_0,a_2} the intrinsic state stemming from our constrained HFB calculations. These $|IM\alpha\rangle$ states are directly used to calculate the reduced transition probability for $E2$ transitions which is written using standard notations as

$$B(E2;\alpha I\rightarrow\alpha' I') = \sum_{\mu,M'} |\langle \alpha' I' M'|\mathcal{M}(E2,\mu)|\alpha I M\rangle|^2 = (2I+1)^{-1}|\langle \alpha' I'||\mathcal{M}(E2)||\alpha I\rangle|^2. \tag{43}$$

The electric moment $\mathcal{M}(E2,\mu)$ is obtained from the multipole moments of the charge density operator

$$\hat{\rho}=\sum_{i=1}^{Z}\delta(\vec{r}-\vec{r}_i), \tag{44}$$

for which the matrix elements are

$$\langle I'M'\alpha'|\hat{\rho}|IM\alpha\rangle = \sum_{KK'}\int\int f_{I'K'\alpha'}(a_0',a_2')f_{IK\alpha}(a_0,a_2)da_0'da_2'da_0da_2 \times[\varphi^{I'}_{M'K'}(\Omega')\langle\Phi_{a_0',a_2'}|R(\Omega')^{+}\hat{\rho}R(\Omega)|\Phi_{a_0,a_2}\rangle \times\varphi^{I}_{MK}(\Omega)]d\Omega d\Omega'. \tag{45}$$

Evaluating this matrix element exactly is a very difficult task. This is why two approximations have been used in calculations here restricted to transitions between SD states. The first one is the so-called rotational approximation in which one assumes that the intrinsic wave functions are deformed in such way that their overlap in the $(\Omega-\Omega')$ Euler angle coordinates is a delta function, that is setting [74]

$$R(\Omega)^{+}\delta(\vec{r}-\vec{r}_i)R(\Omega')=R(\Omega)^{+}\delta(\vec{r}-\vec{r}_i) \times R(\Omega)R(\Omega)^{+}R(\Omega'),$$

with

$$R(\Omega)^{+}R(\Omega')\simeq\delta(\Omega-\Omega'). \tag{46}$$

The second approximation consists in neglecting the nonlocal matrix elements of the density operator in deformation variables [59]. This approximation can be justified for the case of strong overlaps between vibrational amplitudes. We have checked that this local approximation for the superposition amplitudes is good for any SD→SD level transition. This statement would not hold true for SD→ND level transitions, especially those involved in the decay out of SD bands, which is not treated in the present work.

Following Eqs. (40) and (41), the K component of the vibrational amplitude $g_{IK\alpha}$ is written

$$g_{IK\alpha}(a_0,a_2)=\sum_{j=1}^{N_I}C_j^{I\alpha}A_j^{IK}(a_0,a_2). \tag{47}$$

In the GCM+GOA framework, the K-component of the superposition amplitude $f_{IK\alpha}$ is then obtained from the inverse Gauss transform of $g_{IK\alpha}$, namely,

$$f_{IK\alpha}(a_0,a_2)=\frac{|G|^{1/4}}{\sqrt{2\pi}}\exp\left[-\frac{1}{4}\sum_{i,j=0,2}(G^{-1})_{ij}\frac{\partial^2}{\partial a_i\partial a_j}\right] \times g_{IK\alpha}(a_0,a_2), \tag{48}$$

where the matrix G is defined in Eq. (29) and its determinant labeled as $|G|$. Finally, the $E2$ reduced matrix elements in Eq. (43) is written

$$\langle\alpha'I'||\mathcal{M}(E2)||\alpha I\rangle = (2I+1)^{1/2}(2I'+1)^{1/2}\int{\sum_{K,K'}}' f_{I'K'\alpha'}(a_0,a_2)\rho^{a_0,a_2}_{2,K'-K}(r) \times f_{IK\alpha}(a_0,a_2)D^{1/2}da_0da_2\begin{pmatrix} I' & 2 & I \\ K' & m & K\end{pmatrix}, \tag{49}$$

with

$$\rho^{a_0,a_2}_{2,K'-K}(r)=\sum_i\left\langle\phi_{a_0a_2}\left|\frac{\delta(r-x_i)}{r^2}Y^{\star}_{2,K'-K}(\theta_i,\phi_i)\right|\phi_{a_0a_2}\right\rangle, \tag{50}$$

where (x_i,θ_i,ϕ_i) are the intrinsic coordinates of HFB wave functions. The $B(E2)$ calculations are actually performed using the first order expansion of the exponential operator in Eq. (48), that is,

$$f_{IK\alpha}(a_0,a_2)=\frac{|G|^{1/4}}{\sqrt{2\pi}}\left[1-\frac{1}{4}\sum_{i,j=0,2}(G^{-1})_{ij}\frac{\partial^2}{\partial a_i\partial a_j}\right] \times g_{IK\alpha}(a_0,a_2). \tag{51}$$

Equation (51) is accurate enough for evaluating transition rates between states covering the same portion of the (a_0,a_2) space.

IV. RESULTS FROM HFB CALCULATIONS

Here we discuss the predictions obtained for single-particle (sp) energies, potential energy surfaces, and pairing energies.

A. Single particle properties

Proton and neutron sp energies calculated as functions of axial deformation are useful for the identification of shell gaps. These energies are presently deduced from constrained HFB calculations in which the off-diagonal matrix elements of the pairing fields in the HF basis are turned off. Neglecting these matrix elements, which are usually weak [67], corresponds to a BCS treatment of the self-consistent pairing fields deduced from the D1S interaction. In Fig. 5 are shown the proton and neutron sp energies obtained for ^{194}Hg as functions of axial quadrupole deformation. As can be seen, the gaps taking place at very large elongation ($\beta\sim0.6$ and 0.8) correspond to particle numbers $N=110$ and $Z=80$. These gaps stand at the origin of SD minima in the deformation energy surfaces for the $A\sim190$ region. Their magnitudes falling in the range 1–2 MeV are significantly larger than those predicted in separate works [16,38,39,41].

B. Potential energy surfaces

The potential energy surfaces $\mathcal{V}(\beta,\gamma)$ as defined in Eq. (7) are shown for ^{190,192,194}Hg, ^{192,194,196}Pb, and ^{196,198}Po in Figs. 6, 7, and 8, respectively. In their ground state, the Hg isotopes display slightly oblate shapes ($\beta\sim0.15,\gamma\sim\pi/3$) while for the Pb and Po isotopes spherical and near spherical

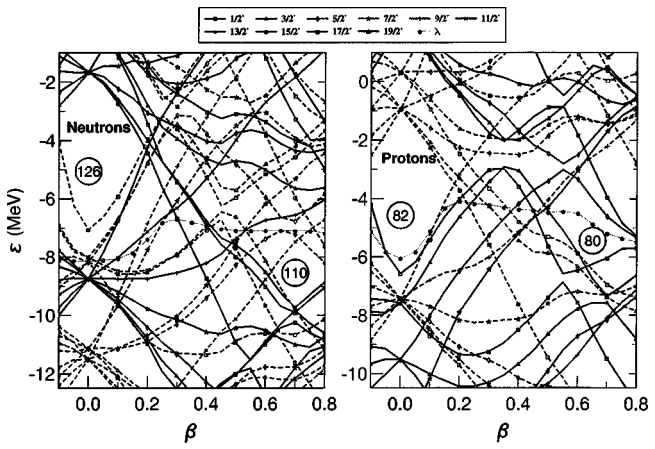

FIG. 5. ^{194}Hg isotope. Neutron (left) and proton (right) single particle energies (MeV) as functions of axial deformation. These are deduced from HFB calculations in which the off-diagonal matrix elements of the pairing fields expressed in the HF basis are ignored. Levels with positive and negative parities are shown as solid and dashed lines, respectively. Codes for spins are given on top of the figure. The Fermi energies are marked with symbols (●) connected by solid lines.

minima are obtained. All these potentials display a secondary axial minimum at large elongation ($\beta\sim0.65$ for the Hg and Pb isotopes, and $\beta\sim0.75$ for the Po isotopes). Furthermore, the SD potentials are (i) more rigid against triaxiality than they are along axial deformation and (ii) their softness in the β coordinate is strongest for the Po isotopes. These landscape properties have important consequences on the excitation energies of $\pi=+$collective vibrations built in the SD potentials. Furthermore, the SD potential well depths are in the range 3–5 MeV. These values are roughly twice as large as those predicted in mean field calculations based on Skyrme forces [38,41] and shell correction method [16]. Part of the observed differences between these predictions and ours stems from that ZPE corrections are included in the present PES calculations.

C. Pairing energies

The proton and neutron pairing energies predicted in our constrained HFB calculations over the sextant $S=(\beta\geqslant0, 0\leqslant\gamma\leqslant\pi/3)$ are shown in Fig. 9 for ^{194}Hg and ^{194}Pb. Strengths are expressed in MeV as indicated by the color codes. The topology of these surfaces is quite complex, reflecting the rich variety of shell effects taking place over the (β,γ) plane. The pairing energies are generally weaker in the region of SD potential minima ($\beta\sim0.65$ and ~0.67 for ^{194}Hg and ^{194}Pb, respectively). The proton pairing energy, in the particular case of ^{194}Hg (and other $Z=80$ nuclei under study), is nearly vanishing in the vicinity of the SD potential minimum. The fact that it does not vanish at no spin preserves the validity of the approximation (23) for the mass parameters, as discussed in Refs. [68,70].

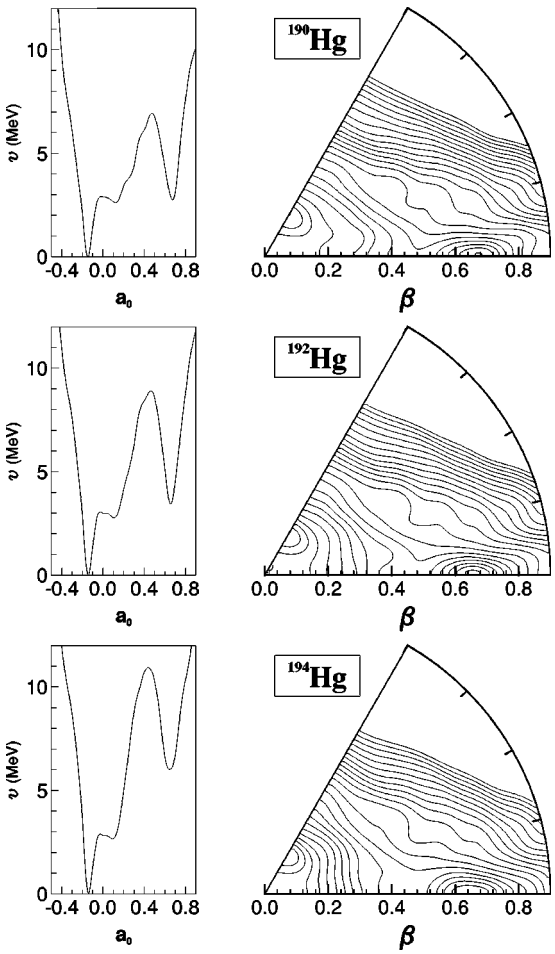

FIG. 6. Right-hand side column: potential energy surfaces (7) as obtained over the sextant $S=(\beta>0,\ 0\leqslant\gamma\leqslant\pi/3)$ from constrained HFB calculations for ^{190,192,194}Hg. Equipotential lines are shown in 1 MeV intervals. Left-hand side column: cuts across these surfaces as functions of the axial deformation a_0.

V. SD LEVEL PROPERTIES

A. Geometrical properties of SD levels

Solving $\hat{\mathcal{H}}_{\rm coll}$ (6) provides a wealth of information on the topology of the wave functions over the (β,γ) plane. In the following discussions, only a few properties will be used for the identification of SD levels among all those predicted in our collective model, namely, (i) the mean β and γ deformations

$$\langle\beta\rangle_{I\alpha}=\int d\Omega\int_S\beta d\beta d\gamma D^{1/2}\Psi^*_{IM\alpha}\beta\Psi_{IM\alpha} \qquad (52)$$

and

$$\langle\gamma\rangle_{I\alpha}=\int d\Omega\int_S\beta d\beta d\gamma D^{1/2}\Psi^*_{IM\alpha}\gamma\Psi_{IM\alpha}, \qquad (53)$$

(ii) the fluctuation parameters

$$\Delta\beta_{I\alpha}=|\langle\beta^2\rangle_{I\alpha}-(\langle\beta\rangle_{I\alpha})^2|^{1/2} \qquad (54)$$

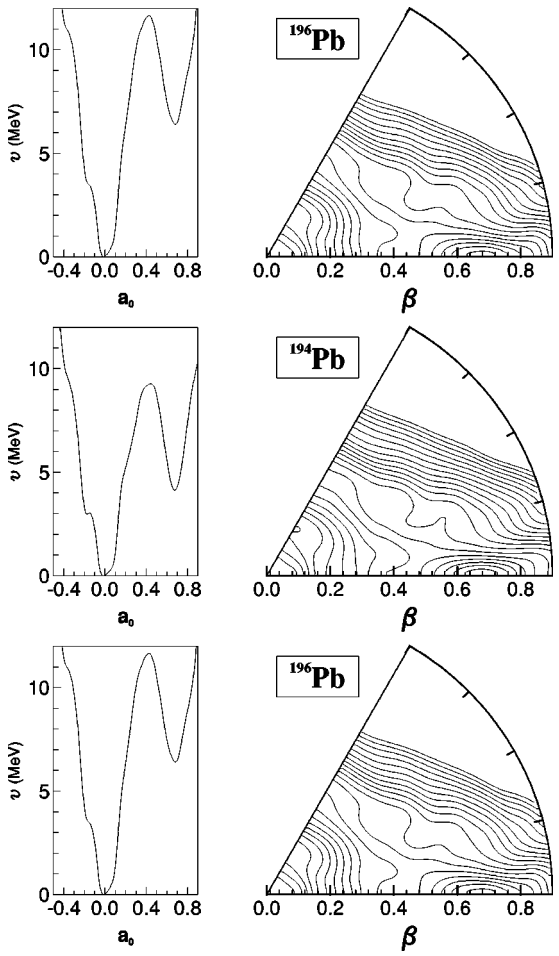

FIG. 7. Same as Fig. 6 for ^{192,194,196}Pb.

and

$$\Delta\gamma_{I\alpha}=|\langle\gamma^2\rangle_{I\alpha}-(\langle\gamma\rangle_{I\alpha})^2|^{1/2}, \tag{55}$$

which measure the spreading of collective states over collective coordinates, (iii) the *K*-component probabilities

$$P_{IK\alpha}=\int_S \beta d\beta d\gamma D^{1/2}|g_{IK\alpha}(\beta,\gamma)|^2, \tag{56}$$

which, as usual in nuclear spectroscopy, serve to decide which states form a rotational or quasirotational band, and (iv) the probability densities

$$\rho_{I\alpha}(\beta,\gamma)=\sum_K |g_{IK\alpha}(\beta,\gamma)|^2 D^{1/2}(\beta,\gamma). \tag{57}$$

We show in Figs. 10, 11, and 12 the systematics of $\pi=+$ collective levels predicted for ^{190,192,194}Hg, ^{192,194,196}Pb, and ^{196,198}Po, respectively. In these (E_x,I) plots, the predictions are marked using various symbols depending upon the values taken by the mean β deformations (52), here labeled for convenience as β_m. Normal deformed (ND) and SD states are shown as dots ($\beta_m<0.2$) and squares ($\beta_m>0.6$), respectively. Levels with intermediate deformation (ID) are also predicted, for which $0.2\leqslant\beta_m\leqslant 0.6$. The ID states with

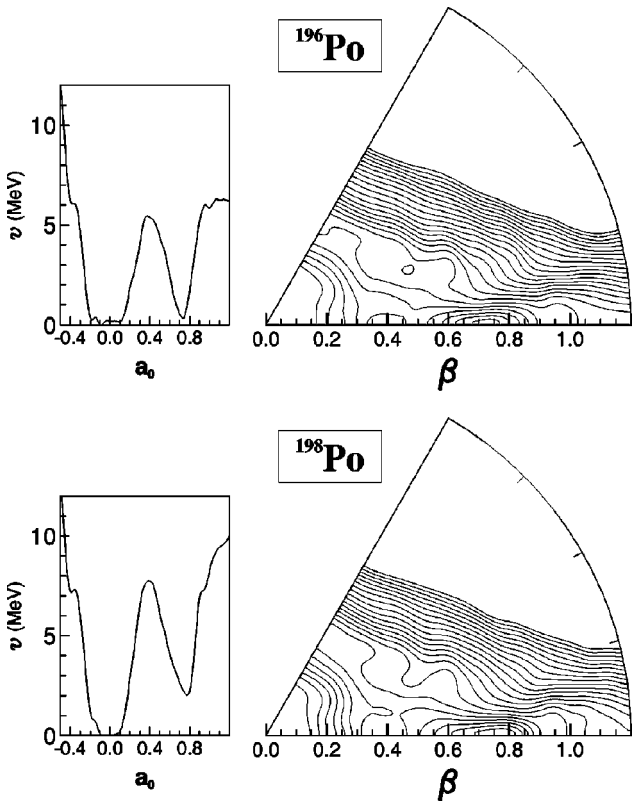

FIG. 8. Same as Fig. 6 for ^{196,198}Po.

mean deformations falling in the intervals $0.2\leqslant\beta_m\leqslant 0.4$ and $0.4<\beta_m\leqslant 0.6$ are shown as pluses and crosses, respectively. These excited ID states form the overwhelming majority among all those predicted below 12 MeV. This analysis extended to the mean γ deformations shows that the SD states

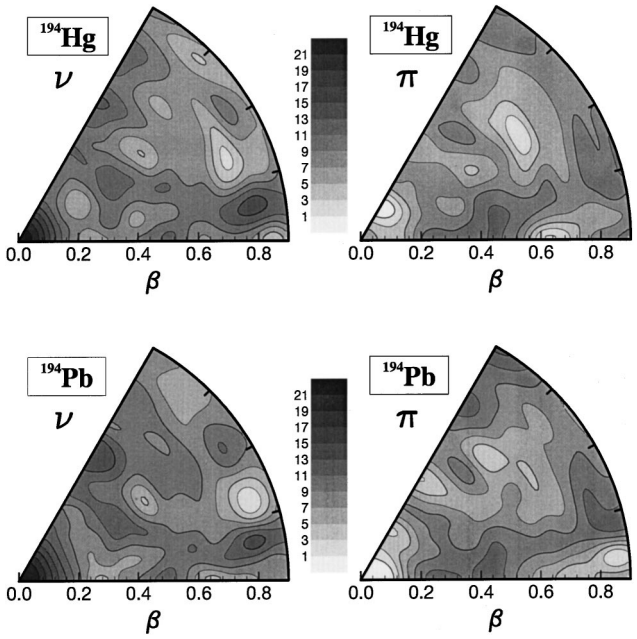

FIG. 9. Proton (π) and neutron (ν) pairing energies from constrained HFB calculations over the sextant S for ^{194}Hg and ^{194}Pb. Codes are for the strengths expressed in MeV units.

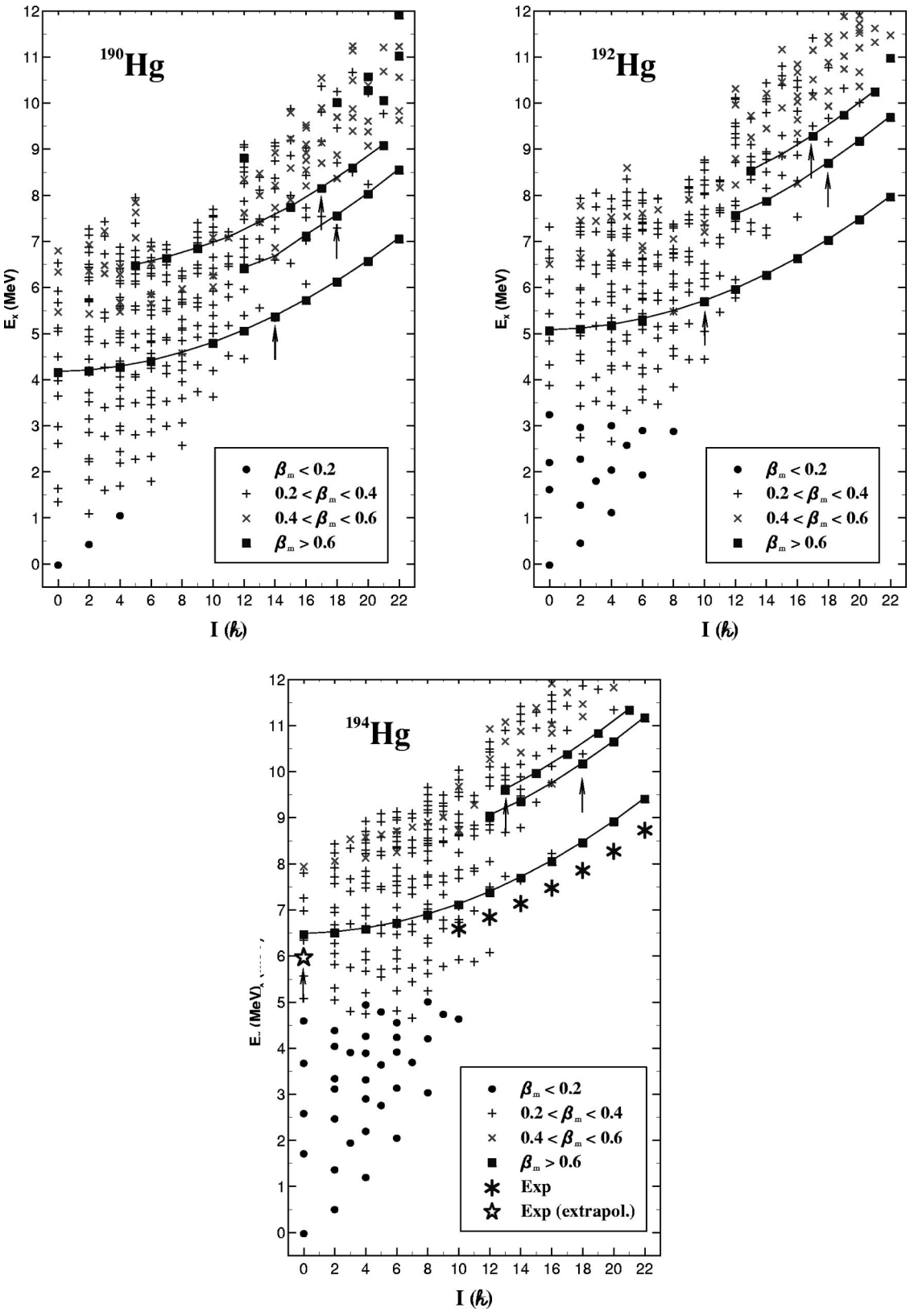

FIG. 10. Solutions of $\hat{\mathcal{H}}_{\rm coll}$ (4) shown up the excitation energy E_x=12 MeV in each spin block from I=0 to I=22 for ^{190,192,194}Hg. The symbols (■), (●), and (+ and ×) mean superdeformed, normal deformed, and intermediate deformed shapes, respectively. From low to high excitation energies are shown (solid lines) our predicted yrast, β, and γ SD bands. Arrows indicate I_c values (see text). Yrast SD states deduced from decay out measurements for ^{194}Hg [75] are marked with asterisk symbols. The open star symbol is for the I=0 shape isomer, as inferred from extrapolation [75].

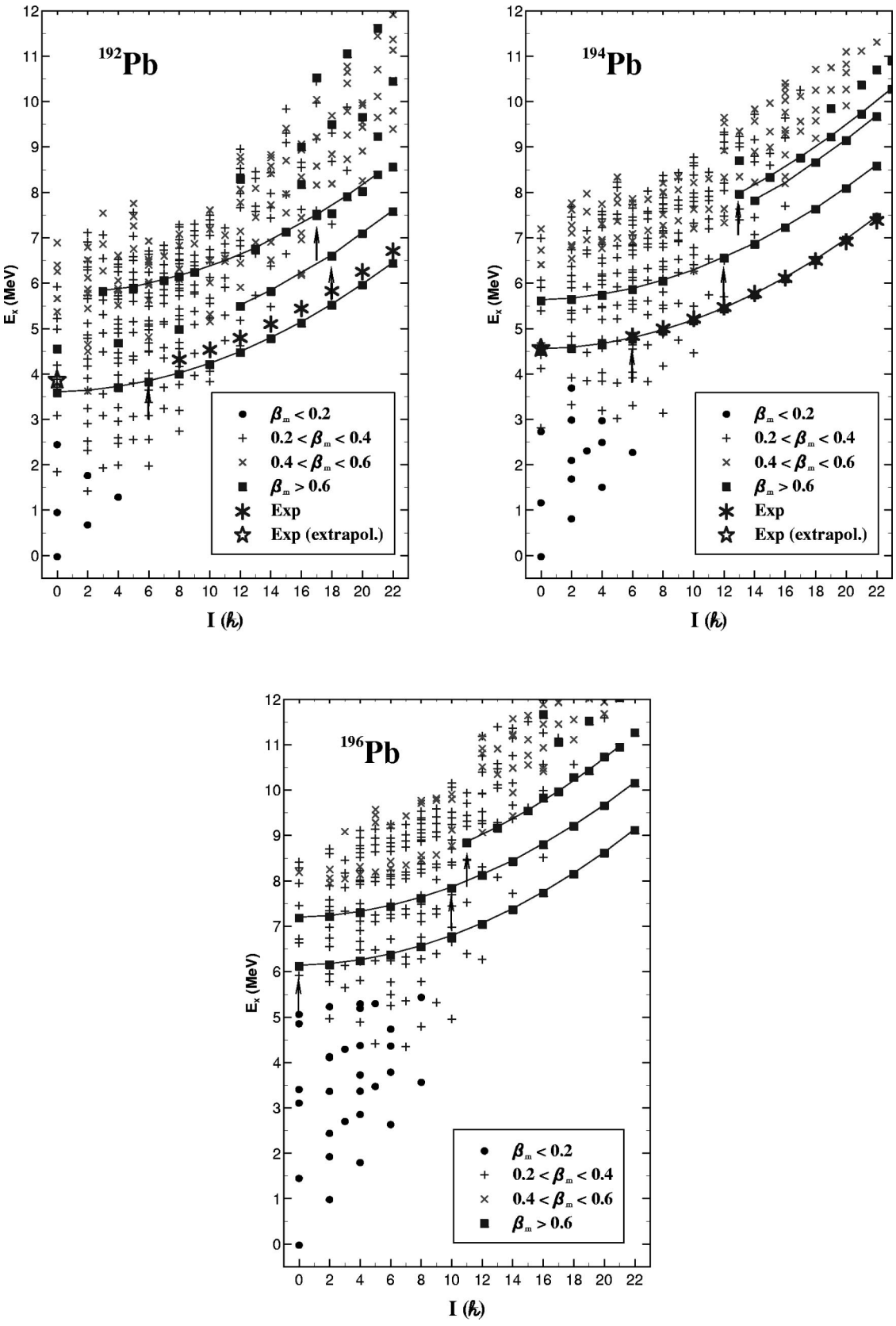

FIG. 11. ^{192,194,196}Pb isotopes. For more details see caption of Fig. 10. The experimental information on yrast SD states and shape isomers for ^{192}Pb and ^{194}Pb are from Refs. [76] and [25,77], respectively.

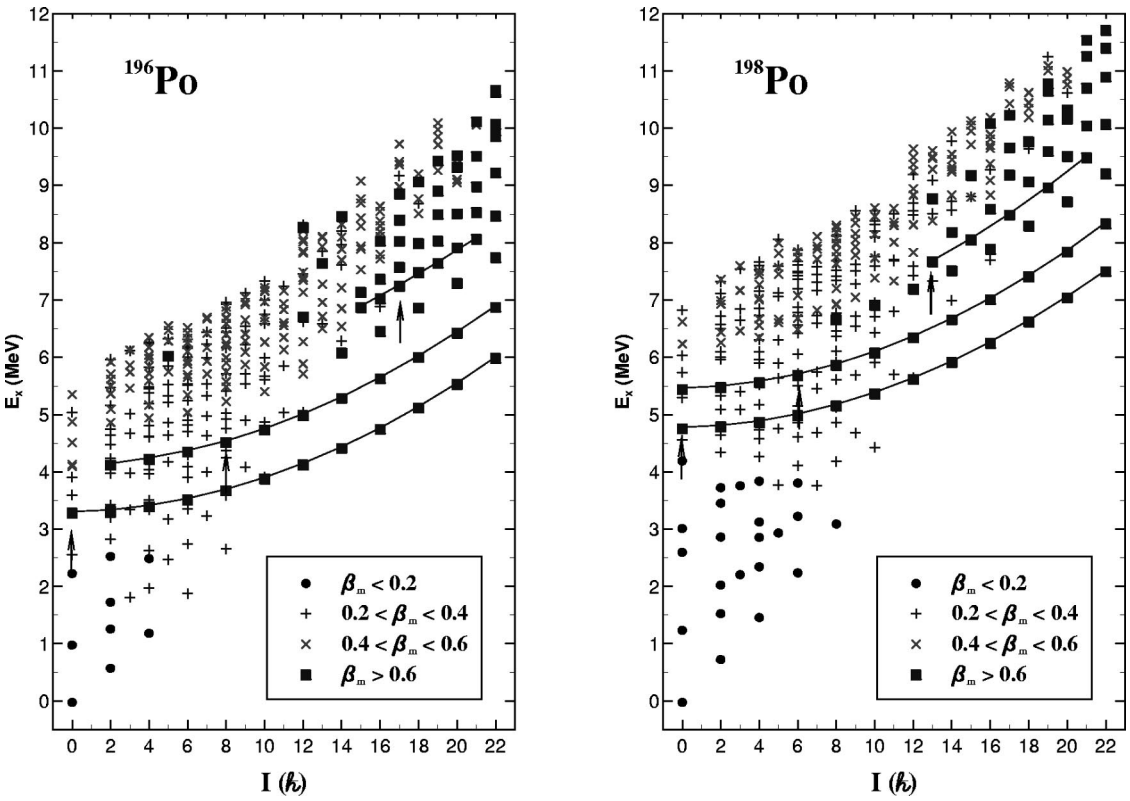

FIG. 12. ^{196,198}Po isotopes. For more details see caption of Fig. 10.

predicted at medium spins ($12 \lesssim I \leqslant 30$) are sharp functions for γ values close to $\gamma = 0°$. Furthermore, their mean deformations $\langle \gamma \rangle_{I\alpha} \sim 3°$ suggest that these SD levels are axially deformed shapes, as illustrated in Fig. 13 through a sample of probability densities calculated for ^{194}Pb and ^{198}Po.

B. SD bands structure

The (E_x, I) plots show that the predicted SD levels form regular patterns as I increases. This feature suggests that the SD states are spread over several bands identified as continuous curves in Figs. 10–12. Whether SD bands may be identified as such may be elucidated through a joint analysis of (i) the mean $\langle \beta \rangle_{I\alpha}$ and $\langle \gamma \rangle_{I\alpha}$ deformations, (ii) the fluctuation parameters $\Delta\beta_{I\alpha}$ and $\Delta\gamma_{I\alpha}$, and (iii) the K-component probabilities $P_{IK\alpha}$. This analysis has been conducted for all the nuclei under consideration.

1. Yrast SD bands

The dominant $K=0$ character is shared by all the yrast SD states. However, this property alone does not guarantee that the yrast SD bands actually exist all the way from high spins down to the $I^\pi = 0^+$ shape isomers (which so far have escaped experimental identification). We adopt the empirical criteria that a band gets broken as soon as a presumed band member is not well localized in the SD potential when I decreases from, say, $I=22$. As an illustration, Fig. 14 shows that the ^{194}Pb yrast SD band (i.e., SD band 1) displays regular mean β and γ deformation properties (solid lines) when the spin decreases down to $I=6$. For $I=4$, the predicted SD level is no longer dominated by its $K=0$ component. Furthermore, the fluctuation parameters $\Delta\beta$ and $\Delta\gamma$ relevant to this level display values which significantly depart from those predicted (spreads around solid lines) for all the SD levels with $I \geqslant 6$. The $I=4$ SD band 1 member mixes with ND and ID levels, which suggests that SD band 1 demises below the critical value $I_c = 6$, prediction marked by an arrow in the lower panel of Fig. 14. Similar analyses conducted for ^{190}Hg, ^{192}Hg, and ^{192}Pb lead to the results: $I_c = 14$, 10 and 6, respectively (see arrows pointing to the yrast SD lines in Figs. 10 and 11). In contradistinction, the yrast SD bands predicted for ^{194}Hg, ^{196}Pb, ^{196}Po, and ^{198}Po display smooth and regular geometrical properties all the way down to their heads, the $I^\pi = 0^+$ shape isomers. This implies that $I_c = 0$.

The $I_c \neq 0$ values here predicted for ^{190,192}Hg and ^{192,194}Pb agree to within two units of angular momentum with experimental information [19,92]. Furthermore, no agreement is found for ^{194}Hg, ^{196}Pb, and ^{198}Po. These contrasted predictions relevant to the spin windows in which the decay out of yrast SD bands takes place, strongly suggest that our empirical criteria are probably too rough to characterize the decay out process [78] and that the present theory should be extended to include qp excitations and/or collective modes not treated in the present work.

2. β bands

The first excited band (SD band 2) predicted in the SD potentials is also dominated by the $K=0$ component. In normally deformed nuclei, this feature indicates that a rotational band is built on top of a β vibration. This physical picture is

valid in the superdeformation regime. Therefore, SD band 2 is interpreted as a β-vibrational band. With the criteria adopted in the analysis of yrast SD levels, these bands terminate at $I_c=18$, 18, 18, 18, 12, 10, 8, and 6 in ^{190}Hg, ^{192}Hg, ^{194}Hg, ^{192}Pb, ^{194}Pb, ^{196}Pb, ^{196}Po, and ^{198}Po, respectively (see arrows in Figs.10–12). For spins lower than I_c, states with SD geometrical properties do exist in most cases. In particular, one-β-phonon states are here predicted at null spin for ^{194,196}Pb and ^{198}Po.

A second $K=0$ vibrational band (SD band $2'$) located at an excitation energy approximately twice that of SD band 2 is predicted at higher spins ($I_c \gtrsim 18$), except for ^{190,192}Hg. This excited SD band, not marked by continuous curves in Figs. 10–12, can be considered as a two-β-phonon band. Whether SD band $2'$ is predicted or not is directly related to the depth and shape of SD potentials and to the strength of collective masses at, and in the vicinity of the SD potential minima.

3. γ bands

SD states with a major $K=2$ component and even spin values are not predicted. In contrast, we are able to identify a sequence of $I=$odd SD levels for which the $K=2$ component dominates. This is a γ-vibrational band, identified as SD band 3, which never extends down to low spins. The band termination takes place at $I_c=17$, 17, 13, 17, 13, 11, 17, and 13 in ^{190,192,194}Hg, ^{192,194,196}Pb, and ^{196,198}Po, respectively. These I_c values are marked by arrows pointing to the higher continuous curves shown in Figs. 10–12.

As a summary of these discussions, the SD states in a band retain their density distributions sharply peaked near the SD potential axial minima until they get weakly or strongly mixed with ID and ND levels when the spin decreases. The sharp character of SD states in the $A\sim 190$ is gained through rotation.

VI. SD BAND PROPERTIES

In this section are presented our model predictions for SD level energies, kinematic moments of inertia, quadrupole moments, and strengths for intraband and interband transitions. Comparisons with measurements are also offered for yrast SD bands.

A. Yrast bands

1. Excitation energies

The excitation energies calculated for the $I=0$ shape isomers are gathered in Table I. For each isotopic chain, there is a clear cut trend in these energies to increase with increasing neutron number. This pattern is to be correlated with variations in the shell and pairing properties at superdeformed shapes, which lead to a gradual shift of the SD potential minima to higher excitation energies. These minima are lowest for $N=110$, the neutron magic number for SD nuclei in the $A\sim 190$ region. We also notice that for each isotonic chain, the predicted shape isomers lower their energies as Z increases. The trends of our predictions over the range $Z=80-84$ and $N=110-114$ are in good agreement with the limited experimental information inferred from decay out studies pertinent to Hg and Pb isotopes. In Table I, spins and excitation energies of SD levels measured at the decay out are also compared with our calculations for $I>0$. These are able to reproduce fairly well the experimental data to within ± 500 keV. The reliability of our calculations has further been assessed for ^{238}U, for which the value $E_x=2.378$ MeV predicted for the $I=0$ shape isomer energy is in very good agreement with $E_x=2.558$ MeV deduced from experiments [83].

2. Decay of SD states

The decay out in the $A\sim 190$ region is dominated by $E1$ transitions [80,84] which are ignored in our collective picture involving only quadrupole collectivity. However, we may study the decay mechanism by calculating the inner potential barriers as functions of spin, and compare our results with those deduced from the phenomenological compound mixing model [85]. In this scenario, it is suggested that the decay mechanism implies both mixing between ND and SD states and persistence of the inner potential barrier. We proceed as follows. First we extract from the collective Hamiltonian $\hat{\mathcal{H}}_{\rm coll}$ (35) the potential energy surface $\mathcal{V}(\beta,\gamma)$ (7). Since we predict that the $K=0$ components by far ($\geqslant 99\%$) dominate the yrast SD level wave functions, next we define in the SD region an axially symmetric potential $\mathcal{V}_I(\beta)$

$$\mathcal{V}_I(\beta)=\mathcal{V}(\beta,\gamma=0)+\frac{\hbar^2}{2\mathcal{J}_x(\beta,\gamma=0)}I(I+1), \qquad (58)$$

where $\mathcal{J}_x$ is the calculated moment of inertia (20). $\mathcal{V}_I$ may be interpreted as the effective potential sustaining the yrast SD state with spin I. This potential calculated over the range $I=0-20$ is shown in Fig. 15 for ^{192}Hg and ^{194}Pb. As can be seen, the SD potentials (solid curves) get deeper as I in-

TABLE I. Predicted and measured excitation energies of yrast SD levels at low spin.

	I^π	$E_{\rm theo}$(MeV)	$E_{\rm exp}$ (MeV)	References
^{190}Hg	0^+	4.18		
	10^+	4.81		
^{192}Hg	0^+	5.08	(5.7 ± 0.5)	[79]
	(10^+)	5.72	(6.8 ± 0.9) ; (6.5 ± 0.9)	[80,81]
^{194}Hg	0^+	6.49	(6.0)	
	10^+	7.13	6.63	[82]
^{192}Pb	0^+	3.61	(3.9)	
	8^+	4.02	(4.357)	[76]
^{194}Pb	0^+	4.55	(4.6)	
	6^+	4.80	4.877	[77]
^{196}Pb	0^+	6.14		
	10^+	6.80		
^{196}Po	0^+	3.30		
	10^+	3.90		
^{198}Po	0^+	4.78		
	10^+	5.39		

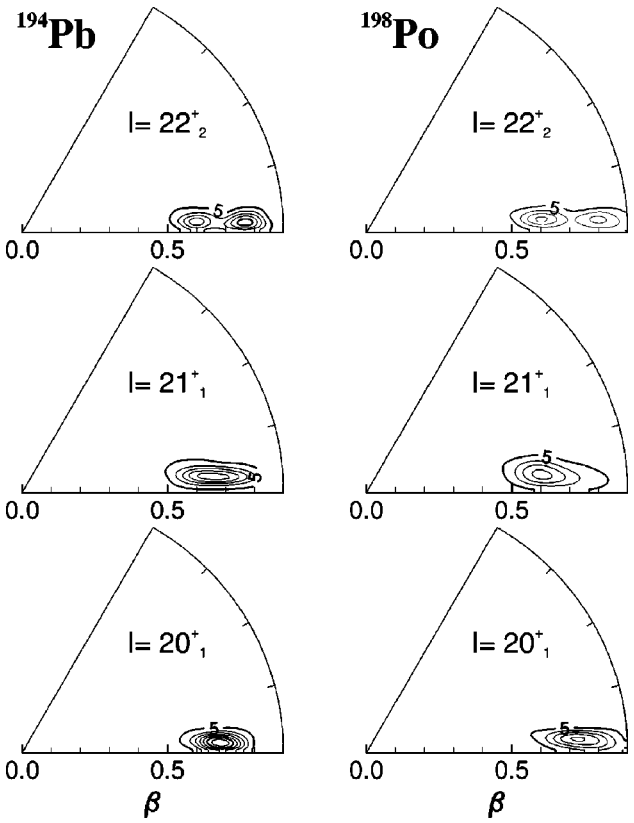

FIG. 13. ^{194}Pb and ^{198}Po isotopes. Probability densities (57) over the sextant S for the SD levels with spin $I=22$, 21 and 20 in the β, γ and yrast SD bands, respectively. Contour lines are separated by 20 units.

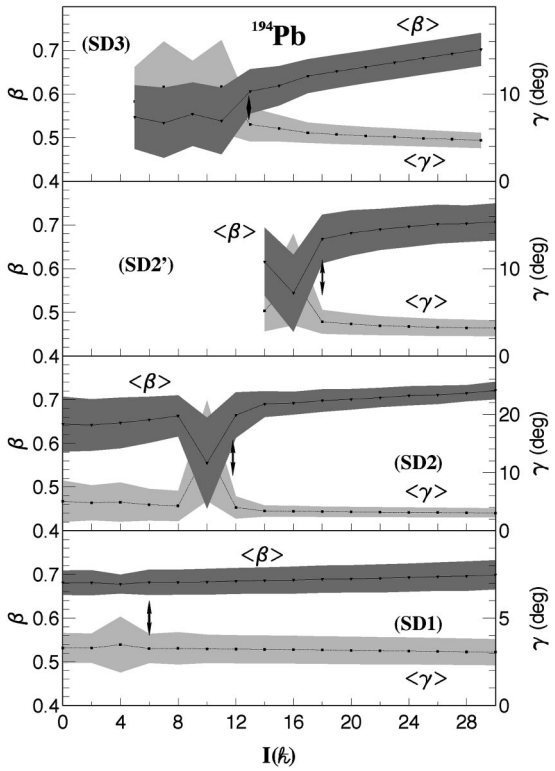

FIG. 14. ^{194}Pb isotope. Mean deformations $\langle\beta\rangle$ and $\langle\gamma\rangle$ (lines) and fluctuation parameters $\Delta\beta$ and $\Delta\gamma$ (shaded areas) for the yrast band (SD1), and β (SD2), $\beta\beta$ (SD2$'$), and γ (SD3) vibrational SD bands. Calculations are for $I\leqslant 30$. The scale at the left-hand side is for mean β deformation, and that for γ deformation is at the right-hand side. Arrows have the same meaning as in Fig. 10.

creases. This property is consistent with that deduced from cranking model calculations. Finally the inner barrier height W_I is defined as

$$W_I=\mathcal{V}_I(\beta_S)-E_x(I), \tag{59}$$

where $E_x(I)$ is the excitation energy of the predicted yrast SD level with spin I (see Figs. 10–12), and β_S the axial deformation ($\beta_S\sim 0.4$) calculated at the top of the inner barrier. As shown in Fig. 16, W_I smoothly increases with increasing spin. Around $I=10$, $W_I\sim 1.3$ MeV for both ^{192}Hg and ^{194}Pb. This value is in excellent agreement with empirical estimates [81,82,86] shown as triangles, crosses, and open diamonds. W_I has also been calculated for the other SD nuclei in our sample. The results, also shown in Fig. 16, suggest that the W_I's are stronger for the Po isotopes than for the Hg and Pb isotopes. This feature of the Po isotopes stems from their very deep $\mathcal{V}_I(\beta)$'s and strong collective masses, which should favor a decay out at low spins.

3. Quadrupole moments

A number of high precision measurements are now available for charge quadrupole moments of yrast SD bands [87–91], which provide opportunities to further challenge our predictions. These data are shown as shaded areas or solid symbols with error bars in Fig. 17, where they are compared with our static and dynamic calculations. The first ones provide $Q_{\rm pot}$ (dashed curves), the charge quadrupole moments at the collective SD potential minima. In the second calculations, Q_t (solid curves) is obtained from our $B(E2)$ predictions using the rotational model assumption. As can be seen, the Q_t values slightly decrease through the γ-ray cascades. This means that the SD shapes are subject to a minor stretching under the influence of rotation. This structure effect would be difficult to measure, except for the ^{196,198}Po isotopes and possibly for ^{192}Pb where it might be as large as 10% over the spin range under consideration. Although the predictions $Q_{\rm pot}\sim Q_t$ is obtained for most yrast SD bands, it may happen that the static calculations provide only rough estimates for quadrupole moments.

4. Moments of inertia

For the yrast SD bands, the kinematic moments of inertia

$$J^{(1)}(I)=\frac{2I-1}{E(I)-E(I-2)} \tag{60}$$

have been deduced from our predicted spectra and compared in Fig. 18 with experimental values inferred from measured E_γ transition energies, and tentative spin assignments [19,92] unless the linking transitions are observed [76,77,75]. As can be seen, the calculated $J^{(1)}$'s remain almost constant when I increases except for ^{198}Po. It is no surprise that constant $J^{(1)}$

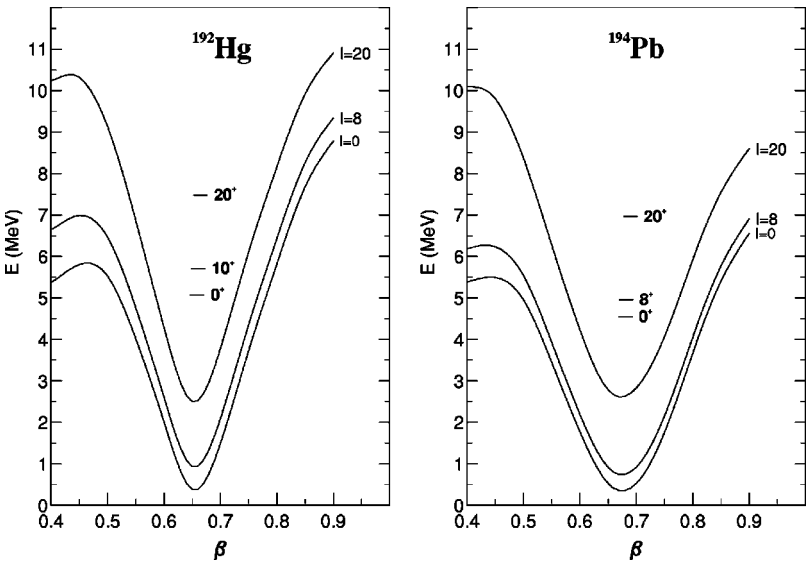

FIG. 15. Effective potentials $\mathcal{V}_I(\beta)$ (58) for the yrast SD states with spins $I=0$, 10, and 20 (^{192}Hg) and $I=0$, 8, 20 (^{194}Pb), and predicted yrast SD levels. The horizontal position of each level corresponds to its mean β deformation.

values are predicted because (i) the mean deformation does not depend upon angular momentum if potential energy surfaces are sharp and deep enough and (ii) the adiabatic approximation embedded in our model ignores the influence of rotation on intrinsic states. For ^{198}Po, the calculated 5% increase of the moment of inertia $J^{(1)}$ is here related only to the stretching effect discussed previously. Our model is indeed unable to predict the rise observed in the experimental $J^{(1)}$ values when I increases. These systematic trends may be understood by relaxing the adiabatic approximation and using instead the self-consistent cranking model (see, e.g., Ref. [51]). However, the GCM+GOA approach is valid at low spins where a comparison between calculated and measured $J^{(1)}$ values is fully justified. At low spins, the predicted and measured $J^{(1)}$ values overlap quite nicely to within 3% on the average, the largest differences between these quantities reaching $\simeq 5\%$ for ^{194}Hg and ^{198}Po. These differences mainly result from our early decision of adopting the value $R_k=1.32$ in the prescription (20) for the moments of inertia entering $\hat{\mathcal{H}}_{\rm coll}$. Releasing this conservative number (as suggested by the crosses shown in Fig. 2) would lead to improving our $J^{(1)}$ predictions, except for ^{198}Po.

Figure 18 also includes the moments of inertia (17) calculated at superdeformed PES minima in the manner of Thouless-Valatin, that is in a mean field approximation for rotation ignoring all the other collective degrees of freedom. These $J^{\rm TV}$ values shown as arrows are systematically 10–20 % larger than the kinematic moments of inertia (60) determined at low spins. These systematic differences observed between $J^{\rm TV}$ and $J^{(1)}$ show that *vibrational correlations* play a key role in the analysis of moments of inertia. Rotation and vibration are not decoupled modes, at low and moderate spins in the $A\sim 190$ region of superdeformation. This is one of the main results of this study.

B. Vibrational SD bands

1. Energies

The relative excitation energies of the β- and γ-vibrational SD bands are shown in Fig. 19. These predictions are based on information inferred from mean deformations (see Sec. V), solid curves in Figs. 10–12, and strengths of $E2$ reduced transition probabilities calculated for intraband transitions (see below). As can be seen, the β vibrations predicted in the SD potentials come first above yrast bands. This means that the superdeformed potentials are softer against elongation than against non axial deformation, properties which propagate on the topology of probability densities (see Fig. 13). None of these bands have so far been observed, partly because they stand (too) high in excitation energy above yrast levels. However, it is for the ^{196,198}Po isotopes that the β-vibrational bands are lowest ($0.8\lesssim E_x\lesssim 1.1$ MeV). Such a β SD band observed at $E_x(\exp)=0.648$ MeV for ^{238}U [93] is predicted by the present model at $E_x(\text{th})=0.97$ MeV, in fair agreement with the experimental value. The relative excitation energies of γ bands are predicted in the range 2.1–2.6 MeV. This property is interpreted as a direct consequence of the stiffness of SD potentials against triaxiality, which should not favor experimental observation. Finally, we notice that the excitation energies here predicted for the β SD bands in Hg and Pb isotopes are systematically lower than those predicted in GCM calculations for the $K^\pi=0^-$ octupole mode [94].

2. Intraband transitions

The $B(E2;I\rightarrow I-2)$ values for transitions between SD states in bands 2 and 3 have been calculated for all the nuclei under study. Whenever needed, these transition rates are explicitly noted as $B(E2;\text{SD2}\rightarrow\text{SD2})$ and $B(E2;\text{SD3}\rightarrow\text{SD3})$, respectively, in the present discussion. For the sake of completeness, the predicted $B(E2;\text{SD1}\rightarrow\text{SD1})$'s relevant to the yrast SD bands are also considered.

A feature common to all SD nuclei but ^{198}Po is that $B(E2;\text{SD1}\rightarrow\text{SD1})$, $B(E2;\text{SD2}\rightarrow\text{SD2})$, and $B(E2;\text{SD3}\rightarrow\text{SD3})$ display similar patterns as I increases: the transition rates in a band increase and reach values common to all three bands as soon as $I\sim 22$. This increase is related to the properties of the 3-j coupling coefficient in Eq. (49), and to the stretching effects discussed previously, which may enhance

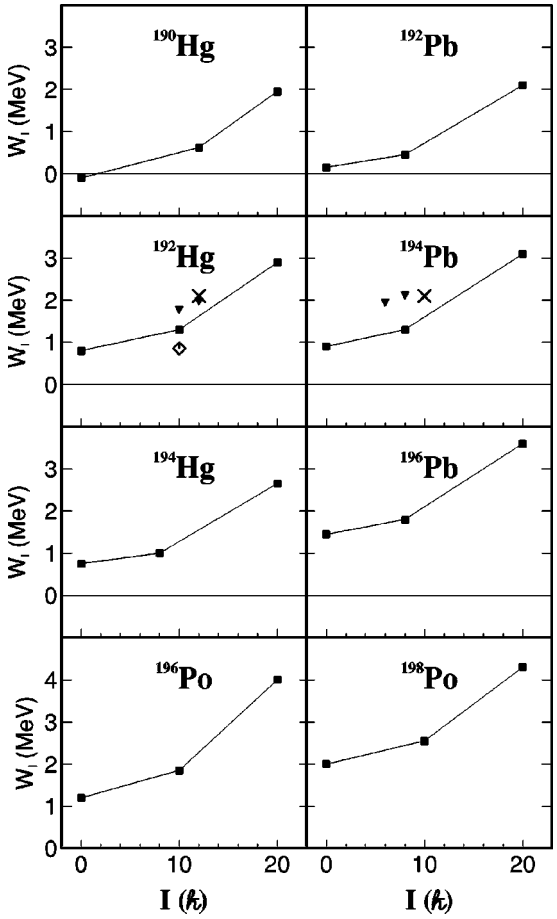

FIG. 16. Predictions (full squares connected with full lines) for the inner potential barrier heights (59) in ^{190,192,194}Hg, ^{192,194,196}Pb, ^{196,198}Po. The symbols ($\diamond$), ($\blacktriangledown$), and ($\times$) are experimental estimates from [81,82,86] and [77,86] for ^{192}Hg and ^{194}Pb, respectively.

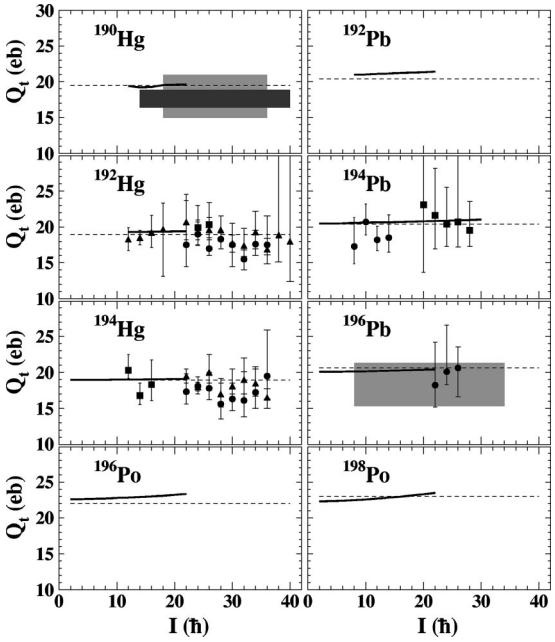

FIG. 17. Quadrupole moments (e b) of yrast SD bands. The dashed and solid curves represent our predictions for static and transition moments, respectively. The shaded areas and various symbols with errors bars are for experimental measurements. The experimental information for ^{190}Hg, ^{192}Hg, ^{194}Hg, ^{194}Pb, and ^{196}Pb are from Refs. [87], [88], [89], [90], and [91], respectively. For ^{196}Pb the adopted spins are two units of angular momentum higher than those of Ref. [91], and therefore consistent with those in Ref. [19]. The three individual Q_t values [91] (full circles) have been renormalized accordingly.

the phenomena. An illustration is shown for ^{194}Pb in the lower panel of Fig. 20 where the $B(E2)$ value common to all three bands is $B_c(E2)\sim 2400$ Weisskopf units (W.u.). Similar strengths are obtained for ^{192,196}Pb. As a general statement, it can be said that $B_c(E2)$ gradually increases from 2000 W.u. (Hg isotopes) to 2800 W.u. (^{196}Po).

The ^{198}Po nucleus displays rather different properties at superdeformation. In addition to the obvious stretching effect on the $B(E2;\ \mathrm{SD1}\rightarrow\mathrm{SD1})$ values, we also observe in the lower panel of Fig. 20 that the three $B(E2)$ sets show a spread of magnitudes which does not reduce significantly when I increases up to $I=22$. This spread of $B(E2)$ values can be traced back to the topology of probability densities shown in Fig. 13. In the vicinity of $I=22$, we see that the ^{198}Po densities for SD levels with spins $I=20$ (SD band 1), 21 (SD band 3) and 22 (SD band 2) are peaking at different deformations. It would be interesting to extend the calculations to check whether $B(E2;\ \mathrm{SD1}\rightarrow\mathrm{SD1})$, $B(E2;\ \mathrm{SD2}\rightarrow\mathrm{SD2})$, and $B(E2;\ \mathrm{SD3}\rightarrow\mathrm{SD3})$ take on closer values at higher spins.

3. Interband transitions

The $B(E2)$ values calculated for transitions between SD band n and SD band m are expressed using the notation $B(E2;\ \mathrm{SD}n\rightarrow\mathrm{SD}m)$. Their strengths are displayed for ^{194}Pb and ^{198}Po in the upper parts of Fig. 20 where the symbol $\Delta I=0$, 1, and 2 means spin transfer up to two units of angular momentum.

The predictions shown for ^{194}Pb are representative of the interband transition properties of ^{190,192,194}Hg, ^{192,196}Pb, and ^{196}Po. First, we observe that $B(E2;\ \mathrm{SD2}\rightarrow\mathrm{SD1})$ remains approximately constant over the spin range $I\leqslant 30$. This prediction does not depend upon whether $\Delta I=0$ (open circles) or $\Delta I=2$ (dots). The $B(E2)$ strength is ~ 10 W.u. This strong value together with excitation energies in the MeV range (see Fig. 19) are not favorable to the observation of β-vibrational bands in most SD nuclei of the $A\sim 190$ region. The γ-vibrational bands would be even more difficult to observe because (i) their excitation energies are high [$E_x(\gamma)\approx 2E_x(\beta)$] and (ii) their main decay paths proceeding through SD3$\rightarrow$SD1 transitions involve $B(E2)$ rates approximately ten times stronger than those for the β-vibrational band decay (see top of Fig. 19). This difference between $B(E2)$ strengths may be understood by considering the difference in shape between the density probabilities of the initial β and γ SD levels (see Fig. 13).

Following the same method of reasoning now for ^{198}Po, we deduce that the decay properties predicted for the γ-vibrational band do not favor experimental identification. In contrast, the $B(E2;\ \mathrm{SD2}\rightarrow\mathrm{SD1})$ rate predicted for the stretched (i.e., $\Delta I=2$) transitions gets weaker as I increases

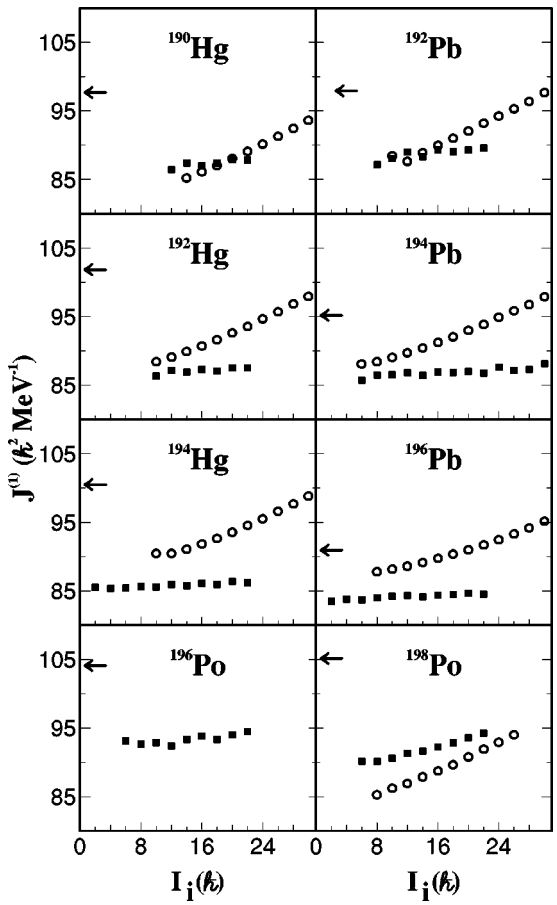

FIG. 18. Kinematic moments of inertia of yrast SD bands. Comparison between our predictions (full squares) and values inferred from measurements (circles). The arrows indicate the moment of inertia calculated *á la* Thouless Valatin (see text). The ''experimental'' $J^{(1)}$ values are deduced from measurements and spin assignments gathered in Ref. [19].

and reaches the value $B(E2)=4$ W.u. for $I=22$. This prediction together with the expected low excitation energy $E_x(\beta) \sim 800$ keV (see Fig. 19) should favor the experimental discovery of a low-lying β-vibrational SD band in ^{198}Po.

4. Moments of inertia

Before closing this presentation relevant to the excited band properties, we now briefly discuss our results for kinematic moments of inertia. For all nuclei but ^{198}Po, the $J^{(1)}$ values predicted for excited and yrast SD bands are nearly identical and show no significant variations with increasing spin. In contrast, the kinematic moment of inertia predicted for the excited and yrast SD bands of ^{198}Po display a common pattern: their values increase at the same rate when I increases. Furthermore, $J^{(1)}(\beta$ band) $[J^{(1)}(\gamma$ band)] is 5% (15%) lower than $J^{(1)}$(yrast band). All these features are not unexpected. They again reflect the influence of stretching effects and vibration correlations on the moments of inertia.

VII. CONCLUSIONS

A general and powerful two-center basis method has been designed and applied to solve a collective Hamiltonian $\hat{\mathcal{H}}_{\rm coll}$ for even-even nuclei showing secondary minima at large elongation in their potential energy surfaces. The collective Hamiltonian under present consideration is built from the GCM+GOA method to describe both rotation and quadrupole vibrations at normal and SD shapes. $\hat{\mathcal{H}}_{\rm coll}$ is parameter free since its surface and kinetic energy components are determined only from the self-consistent HFB method in which the Gogny force is used. Here, our treatment of the kinetic energy is improved over that adopted earlier [46,47], by scaling the Inglis-Belyaev moments of inertia to those calculated in the manner of Thouless-Valatin.

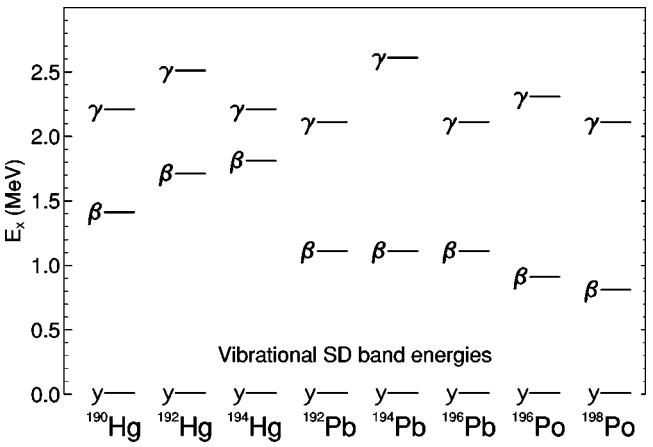

FIG. 19. Relative excitation energies of one-phonon, β, and γ SD bands.

The present study is focusing on the spectroscopic properties of the ^{190,192,194}Hg, ^{192,194,196}Pb, and ^{196,198}Po isotopes at large deformation. Among all the $\pi=+$ collective levels predicted with our methods, only a few display a SD character. The geometric properties attached to the SD levels are exploited to show that these states form yrast and excited SD bands. One-quadrupole-phonon, β and γ SD bands are identified at relatively low excitation energies above the yrast SD bands for all nuclei. These excitation energies depend upon the SD potential shapes and depths. Since the SD potentials are softer along axial deformation than they are against triaxial coordinate, the β bands are systematically lowest in energy. Only for the ^{196}Po and ^{198}Po isotopes are the excitation energies falling below $E_x=1$ MeV. This low excitation energy range should favor experimental discovery of such one-quadrupole-phonon SD bands in the $A\sim 190$ region. The weak $B(E2)$ strengths calculated for stretched $E2$ transitions depopulating the β bands enhance this conclusion for ^{198}Po. In contrast, both excitation energies of γ bands ($E_x=2.1$–2.6 MeV) and strong $B(E2)$'s for γ to yrast band transitions are not favorable properties.

The main trust in our study has been placed on the yrast SD bands for which (i) a wealth of measurements is available and (ii) a decay scenario based on a tunneling process has been suggested. We predict that the yrast SD bands should exist down to the $I=0$ shape isomers. For ^{192}Pb, ^{194}Hg, and ^{194}Pb, their excitation energies compare rather well with those inferred from decay out measurements. Furthermore, the relative excitation energies of $I\sim 10$ levels as estimated for ^{192}Hg and ^{194}Pb above the inner potential barrier invoked

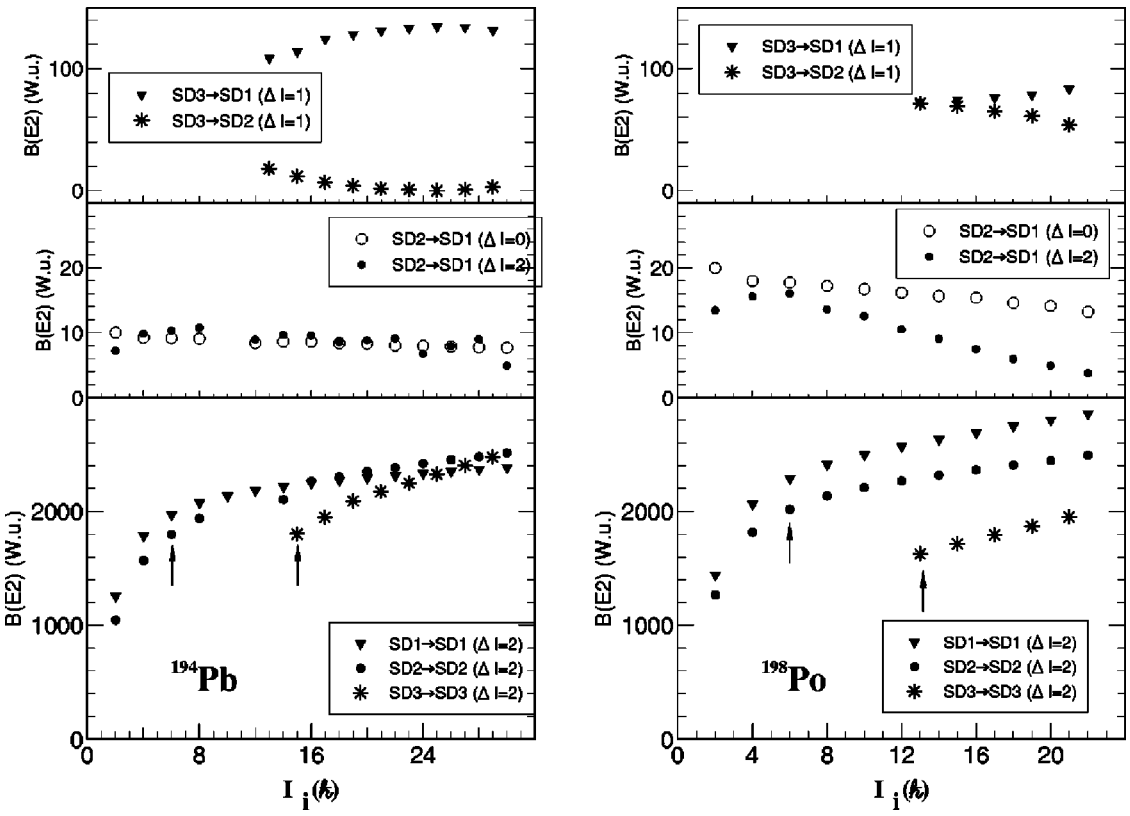

FIG. 20. $B(E2)$ values (in W.u.) predicted for interband and intraband transitions relevant to the yrast, β, and γ SD bands of ^{194}Pb and ^{198}Po. The arrows have the same meaning as in Fig. 10.

in the phenomenological tunneling model, are consistent with our predictions. It would be interesting to measure Q_t for ^{198}Po, the nucleus for which a 10% stretching in its shape is predicted when the spin increases up to $I=22$.

When deduced from our predicted energy spectra, the kinematic moments of inertia $J^{(1)}$ for SD bands are generally constant as functions of spin. This feature is consistent with the adiabatic approximation underlying the GCM+GOA approach. For ^{198}Po, the calculated $J^{(1)}$ values are raising with I, a property which is not correlated with Coriolis coupling. Our $J^{(1)}$ predictions help fixing the spins of observed yrast SD bands. Once the spin assignment has been performed, the experimental and predicted $J^{(1)}$ values overlap within 5% at low spins, except for ^{198}Po. Any other spin assignments would destroy this agreement. This detailed discussion suggests that the two-center basis method together with the microscopic inputs (potential and tensor of inertia) entering our collective model lead to reliable $J^{(1)}$ predictions at low spin. Therefore, the 10–15 % reduction observed when comparing the moment of inertia calculated in the manner of Thouless-Valatin with those deduced from the predicted energy spectra directly stems from quadrupole vibrational correlations. This sizeable effect of rotation-vibration coupling at superdeformed shapes is, in our view, one of the most significant conclusion of the present study. In a forthcoming paper, the rotation-vibration coupling will be discussed again in the context of the cranking HFB method.

ACKNOWLEDGMENTS

We wish to express our gratitude to Dr. D. Gogny for his continuous interest and stimulating discussions. One of the authors (J.L.) thanks the Service de Physique Nucléaire, Bruyères-le-Châtel, for the support and warm hospitality extended to him during the last stage of this work performed under the cooperation agreement between CEA and Université Bordeaux-I.

APPENDIX: ALGEBRAIC AND NUMERICAL METHODS

The eigenstates $|\Psi_i\rangle$ (39) necessarily possess the space symmetries of $\hat{\mathcal{H}}_{\rm coll}$. To minimize the computational effort, the basis states on which the $|\Psi_i\rangle$'s are expanded are built to include the same symmetries. Since these well-known symmetries are more easily expressed in terms of the polar coordinates β and γ, we forget for a moment that $\hat{\mathcal{H}}_{\rm coll}$ is actually solved for the variables a_0 and a_2. In the first stage of this appendix, symmetries attached to the wave functions are briefly defined and applied to the present problem. The second part is devoted to building a convenient set of basis states which are symmetrized and fulfilling boundary conditions. Finally, the last portion of this appendix is devoted to more technical aspects: basis truncations, numerical integration method for matrix elements, orthonormalization, and optimization of the truncated basis.

1. Symmetries in collective wave functions

As pointed out a long time ago, a function $\mathcal{A}$ expressed in the variables (β,γ,Ω) able to describe an eigenstate of $\hat{\mathcal{H}}_{\rm coll}$ with angular momentum I, and therefore obeying the same symmetry rules, may be written in full generality as

$$\mathcal{A}^{IM}_{\alpha}(\beta,\gamma,\Omega)=\sum_{K}{}' \; F^{I}_{K\alpha}(\beta,\gamma)\varphi^{I}_{MK}(\Omega), \tag{A1}$$

where $\varphi^{I}_{MK}(\Omega)$ is the normalized combination of $\mathcal{D}^{I}_{MK}(\Omega)$ Wigner rotation matrices for angular momentum I, with projections M and K onto the third axis in the laboratory and intrinsic systems, respectively, defined as

$$\varphi^{I}_{MK}(\Omega)=\left[\frac{2I+1}{16\pi^2(1+\delta_{K0})}\right]^{1/2} \times[\mathcal{D}^{I}_{MK}(\Omega)+(-1)^{I+K}\mathcal{D}^{I}_{M-K}(\Omega)], \tag{A2}$$

and where α contains any other indexes distinguishing between states with the same (I,M) quantum numbers.

a. Symmetries $\mathcal{R}_1$, $\mathcal{R}_2$, and $\mathcal{R}_3$

An eigenstate of $\hat{\mathcal{H}}_{\rm coll}$, and therefore under our present hypothesis an $\mathcal{A}^{IM}_{\alpha}$ function, must be invariant under any transformation which relabels the intrinsic axes ξ_1, ξ_2 and ξ_3. The three elementary transformations associated with this relabeling are usually chosen as (i) $\mathcal{R}_1$ which reverses the ξ_2 and ξ_3 axes, (ii) $\mathcal{R}_2$ which is the $\pi/2$ rotation around the ξ_3 axis, and (iii) $\mathcal{R}_3$ which is the $\xi_i\rightarrow\xi_{i-1}$ (*with* $\xi_0=\xi_3$) circular permutation of axes.

As is well known, the $\mathcal{R}_1$ invariance establishes a relationship [see Eq. (A2)] between the $+K$ and $-K$ components of $\mathcal{A}^{IM}_{\alpha}$ and rules out the $K=0$ component when I is odd. The $\mathcal{R}_2$ invariance excludes odd K components for any I value, and implies the following parity condition:

$$F^{I}_{K\alpha}(\beta,-\gamma)=(-1)^{K/2}F^{I}_{K\alpha}(\beta,\gamma). \tag{A3}$$

The invariance of $\mathcal{A}^{IM}_{\alpha}$ under the $\mathcal{R}_1$ and $\mathcal{R}_2$ transformations is secured provided that $F^{I}_{K\alpha}$ obeys Eq. (A3), and that the summation over K [noted as Σ' in Eq. (A1)] is restricted to $0\leqslant K\leqslant I$ if K is even, and to $K\neq 0$ if I is odd. Such conditions exclude the subspace of angular momentum $I=1$.

Let us now consider a component $K=N$ in Eq. (A1), that we write $F^{\pi(N)}(\beta,\gamma)\;\varphi^{I}_{MN}(\Omega)$. The index $\pi(N)$ means that the function $F^{\pi(N)}(\beta,\gamma)$ has to obey the parity condition (A3). As shown in a pioneering work [63], applying the $\mathcal{R}_3$ transformation to any one among such components results in

$$\mathcal{R}_3[F^{\pi(N)}(\beta,\gamma)\varphi^{I}_{MN}(\Omega)] =F^{\pi(N)}\left(\beta,\gamma+\frac{2\pi}{3}\right)\sum_{K}{}'(-1)^{K/2}M^{I}_{NK}\varphi^{I}_{MK}(\Omega), \tag{A4}$$

where M^{I}_{NK} is the symmetric matrix

$$M^{I}_{NK}=2(-1)^{N/2}(1+\delta_{N0})^{-1/2}(1+\delta_{K0})^{-1/2}\mathcal{D}^{I}_{NK}\left(\frac{\pi}{2},\frac{\pi}{2},\pi\right), \tag{A5}$$

in which [95]

$$\mathcal{D}^{I}_{NK}\left(\frac{\pi}{2},\frac{\pi}{2},\pi\right) =\frac{(-1)^{K/2}}{2^{I}}\times\sum_{S}\;(-1)^{I-S} \times\frac{[(I+K)!(I-K)!(I+N)!(I-N)!]^{1/2}}{S!(K+N+S)!(I-K-S)!(I-N-S)!}, \tag{A6}$$

where the summation over S runs over values for which factorial functions are defined.

These matrices M^{I}_{NK} obey various relationships deduced from orthogonality properties of the Wigner rotation matrices. Two of them are of special importance for the present analysis, namely,

$$(-1)^{N/2}(-1)^{K/2}\sum_{L}{}'\;(-1)^{L/2}M^{I}_{NL}M^{I}_{LK}=M^{I}_{NK}, \tag{A7}$$

and

$$(-1)^{N/2}(-1)^{K/2}\sum_{L}{}'\;M^{I}_{NL}M^{I}_{LK}=\delta_{NK}. \tag{A8}$$

As shown in Eq. (A4), the $\mathcal{R}_3$ transformation mixes the K components and intricates their relative weights. As a well known result, an $\mathcal{R}_3$ invariant state will necessarily contain all the available K components in the considered subspace of angular momentum I.

b. Functions invariant under $\mathcal{R}_1$, $\mathcal{R}_2$, and $\mathcal{R}_3$

Since $\mathcal{R}_3$ (i.e., the circular permutation of the three principal axes in the intrinsic system of coordinates) has the trivial property $(\mathcal{R}_3)^3=1$, we may define the symmetrization operator $\mathcal{P}_3$ as

$$\mathcal{P}_3=1+\mathcal{R}_3+\mathcal{R}_3^2. \tag{A9}$$

For any function f, $\mathcal{P}_3 f$ is obviously invariant under $\mathcal{R}_3$ and fulfills the property

$$\mathcal{R}_3(\mathcal{P}_3 f)=\mathcal{R}_3(f+\mathcal{R}_3 f+\mathcal{R}_3^2 f)=(\mathcal{R}_3 f+\mathcal{R}_3^2 f+\mathcal{R}_3^3 f)=\mathcal{P}_3 f. \tag{A10}$$

To establish the $\mathcal{P}_3$ operator properties for our particular state functions, we first need to find an explicit form for $\mathcal{R}_3^2$. Applying twice Eq. (A4) to $[F^{I}_{K\alpha}(\beta,\gamma)\varphi^{I}_{MK}(\Omega)]$, and using the property (A7) results in

$$\mathcal{R}_3^2[F^{\pi(N)}(\beta,\gamma)\varphi^I_{MN}(\Omega)] = F^{\pi(N)}\left(\beta,\gamma+\frac{4\pi}{3}\right)(-1)^{N/2}\sum_K{}' \; M^I_{NK}\varphi^I_{MK}(\Omega). \tag{A11}$$

Next, using Eq. (A4) three times together with the property (A8), a transformation compatible with the property $\mathcal{R}_3^3=1$ results in

$$\mathcal{R}_3^3[F^{\pi(N)}(\beta,\gamma)\varphi^I_{MN}(\Omega)] = F^{\pi(N)}(\gamma+2\pi)\sum_K{}' \; \delta_{NK}\varphi^I_{MK}(\Omega), \tag{A12}$$

which is valid as long as

$$F^{\pi(N)}(\beta,\gamma+2\pi)=F^{\pi(N)}(\beta,\gamma). \tag{A13}$$

Of course Eq. (A13) holds true for any univalued function in the deformation space described by the polar variables (β,γ).

Finally, we check that $\mathcal{P}_3[F^{\pi(N)}(\beta,\gamma)\varphi^I_{MN}(\Omega)]$ is also $\mathcal{R}_1$ and $\mathcal{R}_2$ invariant. Considering the explicit form of the $\mathcal{P}_3$ transformation [see Eqs. (A4), (A9), and (A11)], it is easy to check that $\mathcal{P}_3[F^{\pi(N)}(\beta,\gamma)\varphi^I_{MN}(\Omega)]$ has the proper K components [i.e., $(0\leqslant K\leqslant I$, K=even) and ($K\neq 0$ for I=odd)]. It remains to check that the K components

$$\{\mathcal{A}^{IM}_N(\beta,\gamma,\Omega)\}_K=\{\mathcal{P}_3[F^{\pi(N)}(\beta,\gamma)\varphi^I_{MN}(\Omega)]\}_K \tag{A14}$$

of $\mathcal{P}_3[F^{\pi(N)}(\beta,\gamma)\varphi^I_{MN}(\Omega)]$ fulfill the parity condition (A3). Using the relations (A4), (A9), and (A11), we deduce

$$\{\mathcal{A}^{IM}_N(\beta,\gamma,\Omega)\}_K = \delta_{NK}F^{\pi(N)}(\beta,\gamma)+M^I_{NK}\left[(-1)^{K/2}F^{\pi(N)}\left(\beta,\gamma+\frac{2\pi}{3}\right)+(-1)^{N/2}F^{\pi(N)}\left(\beta,\gamma-\frac{2\pi}{3}\right)\right], \tag{A15}$$

from which it is easy to show that

$$\{\mathcal{A}^{IM}_N(\beta,-\gamma,\Omega)\}_K=(-1)^{K/2}\{\mathcal{A}^{IM}_N(\beta,\gamma,\Omega)\}_K. \tag{A16}$$

As a result, the function $\mathcal{P}_3[F^{\pi(N)}(\beta,\gamma)\varphi^I_{MN}(\Omega)]$ built to be invariant by the $\mathcal{R}_3$ transformation, is also $\mathcal{R}_1$ and $\mathcal{R}_2$ invariant.

2. Building a set of symmetrized basis functions

So far, the function $F^{\pi(N)}(\beta,\gamma)$ has been given no close form. We only know that $F^{\pi(N)}$ should fulfill the parity condition (A3), and be an analytic function when expressed in Cartesian coordinates (a_0,a_2). Several ways of adopting a particular close form exist (see, for instance Ref. [96]). Here, we have made our choice through the consideration that $\mathcal{P}_3$ operates on the polar coordinate γ. This feature together with the property (A13) suggest a periodic function in the γ coordinate. Therefore, the basis functions we have adopted [46,47] have the following form:

$$F^{\pi(N)}(\beta,\gamma)\varphi^I_{MN}(\Omega)=Q_\mu[\beta^2,\beta^3\cos(3\gamma)]\beta^m\Phi^{IM}_{Nn}(\gamma,\Omega), \tag{A17}$$

where

$$\Phi^{IM}_{Nn}(\gamma,\Omega)=\cos(n\gamma)\varphi^I_{MN}(\Omega) \quad \left(\frac{N}{2}=\text{even}\right)$$

and

$$\Phi^{IM}_{Nn}(\gamma,\Omega)=\sin(n\gamma)\varphi^I_{MN}(\Omega) \quad \left(\frac{N}{2}=\text{odd}\right), \tag{A18}$$

in which n is a non-negative integer. The function Q_μ does not depend upon the angular variable Ω. For such functions, the $\mathcal{R}_3$ transformation is nothing but making the change $\gamma\rightarrow\gamma+2\pi/3$. The invariants of the $\mathcal{R}_3$ transformation for functions analytic in the (a_0,a_2) coordinates are β^2 and $\beta^3\cos(3\gamma)$ [63]. The function Q_μ which indeed depends only upon these two invariants is not changed by the $\mathcal{P}_3$ symmetrization operator. As discussed later on, the $\mathcal{P}_3$ invariant Q_μ function is taken as an exponential weight which secures the fulfillment of boundary conditions at far edge ($\beta\rightarrow\infty$).

Furthermore, the term β^m is subject to the condition

$$m=n+2\lambda, \tag{A19}$$

where λ is any non-negative integer. This condition guarantees that the basis functions (A17) keep their analytic character when transformed back from the (β,γ) to the (a_0,a_2) coordinates. In numerical applications, m is subject to the cutoff condition $m\leqslant m_{\max}$. Therefore, Eq. (A19) implies the truncation $n\leqslant m_{\max}$.

Next, we build the symmetrized basis functions

$$\mathcal{A}^{IM}_{\mu mNn}(\beta,\gamma,\Omega)=Q_\mu[\beta^2,\beta^3\cos(3\gamma)]\beta^m\{\mathcal{P}_3\Phi^{IM}_{Nn}(\gamma,\Omega)\}, \tag{A20}$$

on which the collective wave functions $\Psi_{IM\alpha}$ (40) are expanded. These are written

$$\Psi_{IM\alpha}(\beta,\gamma,\Omega) = \sum_{\mu=1}^{\mu_{\max}}\sum_{n=1}^{m_{\max}}\sum_{m=n,n+2\cdots}^{m_{\max}}\sum_N{}' \; U^{IM\alpha}_{\mu mNn}\mathcal{A}^{IM}_{\mu mNn}(\beta,\gamma,\Omega), \tag{A21}$$

where α is a label index for a state in the spin block I, and $U^{IM\alpha}_{\mu mNn}$ an expansion coefficient. The $\mathcal{A}^{IM}_{\mu mNn}$ states are not linearly independent. Some of them will be excluded later on using simple algebraic considerations as well as the Gramm-Schmidt method.

a. $\mathcal{P}_3$ transformation in the $\Phi^{IM}_{Nn}(\gamma,\Omega)$ space

In a subspace with angular momentum I, the $\mathcal{P}_3$ transformation is also written

$$\mathcal{P}_3\Phi^{IM}_{Nn}=\sum_K{}' \; C^I_{NKn}\Phi^{IM}_{Kn}, \tag{A22}$$

where the coefficients C^I_{NKn}

$$C^I_{NKn}=\delta_{NK}+M^I_{NK}\Bigg[[(-1)^{N/2}+(-1)^{K/2}]\cos\left(n\frac{2\pi}{3}\right) +(-1)^{N/2}-(-1)^{K/2}\sin\left(n\frac{2\pi}{3}\right)\Bigg] \tag{A23}$$

are deduced from the transformation properties (A9), (A4), and (A11) and from the definition (A18). These results mean that, for a given frequency index n, the space spanned by the $\mathcal{P}_3\Phi^{IM}_{Nn}$'s is a subspace of that spanned by the Φ^{IM}_{Nn} vectors.

The structure of Eq. (A23) has important implications: it renders possible an important reduction of the configuration space. As an example, let us consider the $\mathcal{P}_3$ transformation in the $I=0$ subspace. We obtain $\mathcal{P}_3\Phi^{I=M=0}_{N=0,n=3k+1}=0$ and/or $\mathcal{P}_3\Phi^{I=M=0}_{N=0,n=3k+2}=0$, with k as a non-negative integer. Furthermore, only the components $\mathcal{P}_3\Phi^{I=M=0}_{N=0,n=3k}$ remain. More generally, the C^I_{NKn} properties imply that linear relationships exist between the $\mathcal{P}_3\Phi^{IM}_{Nn}$'s when N is taken as the running index. For instance, $\mathcal{P}_3\Phi^{2M}_{23k+1}=\mathcal{P}_3\Phi^{2M}_{03k+1}$ in the $I=2$ subspace. Furthermore, any component of the form $\mathcal{P}_3\Phi^{2M}_{0n=3k}$ vanishes. Finally, only the components $\mathcal{P}_3\Phi^{2M}_{0n=3k+1}$ and $\mathcal{P}_3\Phi^{2M}_{0n=3k+2}$ need to be considered. These $\mathcal{P}_3$ transformation properties are therefore of some practical importance, as discussed in the following paragraph.

b. Exclusion of useless $\mathcal{A}^{IM}_{\mu mNn}$ basis states

In each block (I,n), we define the number $\mathcal{N}^I_n$ of independent components $\mathcal{P}_3\Phi^{IM}_{Nn}$ as the number of basis elements extracted from the N-ordered lists

$$\{\mathcal{P}_3\Phi^{IM}_{Nn},(N=0,2,4,\ldots I), \quad I=\text{even}\}, \tag{A24}$$

and

$$\{\mathcal{P}_3\Phi^{IM}_{Nn},(N=2,4,6,\ldots I-1), \quad I=\text{odd}\}. \tag{A25}$$

The $\mathcal{N}^I_n$ values are shown in Fig. 21. These form two families of broken lines depending upon whether $n=3k$ (solid line) or $n=3k\pm1$ (dashed line). As an example of the lowering in the basis size resulting from the $\mathcal{P}_3$ transformation, we consider the $I=10$ spin block. For this I value, $\mathcal{N}^I_n=2$. This implies that the $N=0$ and $N=2$ components alone survive the $\mathcal{P}_3$ transformation. The $N=4$, 6, 8, and 10 components are therefore excluded because they can be expressed as linear combinations of $N=0$ and $N=2$ components, or vanish identically.

The $\mathcal{N}^I_n$ values in each block (I,n) increase with angular momentum and display regular patterns, whether $n=3k$ or $n=3k\pm1$. Both lines in Fig. 21 exhibit structures which repeat every six units of angular momentum all the way from low to high spins.

The total number N_I of basis states in each spin block as obtained after useless components have been excluded, depends upon the values taken by the upper limits of the summation indexes μ and m in Eq. (A21). In the present study, we adopt the values $\mu_{\max}=2$ and $m_{\max}=36$ (see below), and thus obtain the N_I set identified in Fig. 22 by the symbol INIT. As can be seen, the total number of basis states in-

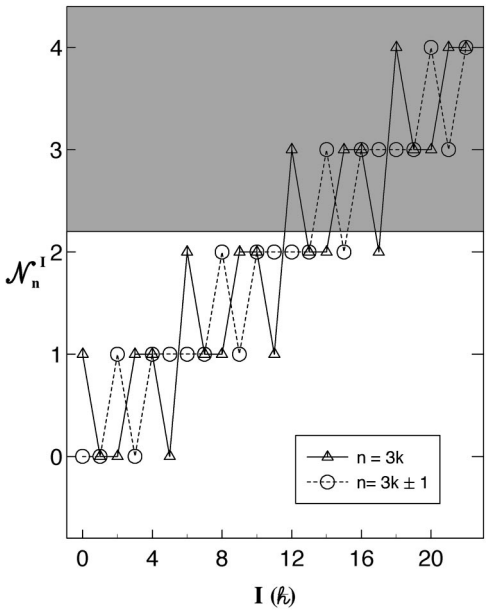

FIG. 21. Number of independent basis components in the block (I,n) as a function of angular momentum and n (see the Appendix). The shaded area means that the truncation $\mathcal{N}^I_n\leqslant2$ is adopted.

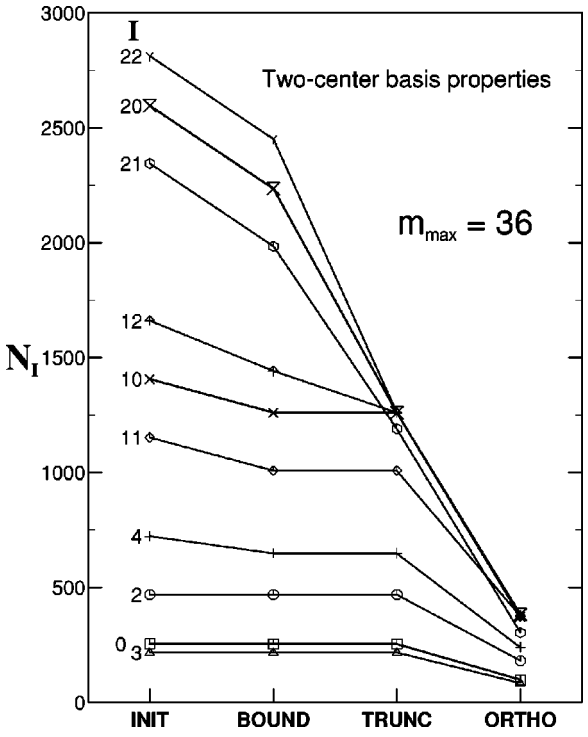

FIG. 22. Number of states considered at different stages labeled INIT, BOUND, and TRUNC while building the $m_{\max}=36$ two-center basis in various spin blocks from $I=0$ to $I=22$. The symbol ORTHO refers to orthonormalized basis sizes found for ^{192}Hg.

creases with spin, from $N_I \sim 250$ ($I = 0$ and 3) to $N_I \sim 2800$ ($I = 22$). Including boundary conditions leads to reducing the N_I values still more, as explained below.

c. Basis functions fulfilling boundary conditions

The boundary conditions dictate that the bound state solutions be vanishing at large elongation (i.e., $\beta \to \infty$). These conditions are fulfilled by taking for Q_μ in Eq. (A20) the exponential form

$$Q_\mu = \exp\left\{ -\frac{1}{2}\{\alpha_{4\mu}(\beta^4) + \alpha_{3\mu}[\beta^3 \cos(3\gamma)] + \alpha_{2\mu}\beta^2\}\right\}, \tag{A26}$$

in which the basis parameters $\alpha_{4\mu}$, $\alpha_{3\mu}$, and $\alpha_{2\mu}$ are properly defined. For any value of the γ coordinate, Q_μ vanishes at far edge provided that either one of the two conditions

$$\alpha_{4\mu} = \alpha_{3\mu} = 0 \quad \text{and} \quad \alpha_{2\mu} > 0 \tag{A27}$$

and

$$\alpha_{4\mu} > 0 \tag{A28}$$

is fulfilled. These conditions will serve as constraints in the numerical method employed later on to optimize the basis parameter sets.

The boundary conditions at axially symmetric shapes (i.e., $\gamma = 0, \pi/3, 2\pi/3$, etc.) have been discussed at length in Ref. [63]. Here, we discuss their impact on the $\mathcal{A}^{IM}_{\mu mNn}$ functions (A20). The discussion restricted to the $\gamma = 0$ and $\gamma = \pi$ cases does not alter the results since the functions (A20) are $\mathcal{R}_3$ invariant. We write the functions (A20) in the convenient form

$$\mathcal{A}^{IM}_j(\beta,\gamma,\Omega) = \sum_K{}' \; A^{IK}_j(\beta,\gamma)\varphi^I_{MK}(\Omega), \tag{A29}$$

where $j = \{\mu, m, N, n\}$, and repeat the analysis *á la* Kumar and Baranger [63] for the $\langle \mathcal{A}^{IM}_j | \hat{\mathcal{H}}_{\rm coll} | \mathcal{A}^{IM}_{j'} \rangle$ matrix elements. After integration over the Euler angles, one is left with integral kernels among which only one needs special care. This kernel is written

$$\sum_{KK'}{}' \int A^{IK}_j(\beta,\gamma) A^{IK'}_{j'}(\beta,\gamma) \frac{K^2 \delta_{KK'}}{\mathcal{J}_3(\beta,\gamma)} d\mu(\beta,\gamma), \tag{A30}$$

where $d\mu$ is the metric and $\delta_{KK'}$ the Kronecker symbol. Problems may arise only for the $K \neq 0$ terms in Eq. (A30). First, we notice that the A^{IK}_j amplitudes with $K/2 =$ odd vanish for $\gamma = 0$ and $\gamma = \pi$ since they are proportional to $\sin(n\gamma)$.

Next, we discuss the case of amplitudes with $K \neq 0$ and $K/2 =$ even, which exist only in the spin blocks $I \geqslant 4$. These amplitudes [proportional to $\cos(n\gamma)$] do not vanish for $\gamma = 0$ and $\gamma = \pi$. When it shows up, this pathology is cured by introducing new basis functions which are linear combinations of the previous ones, namely,

$$\Gamma^{IM}_{\mu mNn} = \mathcal{A}^{IM}_{\mu mNn} + \sigma^I_{Nnn'} \mathcal{A}^{IM}_{\mu mNn'}. \tag{A31}$$

The linear combination (A31) is formed in such way that all the $K \neq 0$ and $K/2 =$ even components of Γ display a γ dependence proportional to $[\cos(n\gamma) - \cos(n'\gamma)]$. This difference vanishes for $\gamma = 0$ and $\gamma = \pi$ only if n and n' have same parity. To find such properties, we need to reexpress Γ (A31) as

$$\Gamma^{IM}_{\mu mNn} = Q_\mu \beta^m [\mathcal{P}_3 \Phi^I_{MNn} + \sigma^I_{Nnn'} \mathcal{P}_3 \Phi^I_{MNn'}]. \tag{A32}$$

Exploiting properties of the C^I_{NKn} coefficients (A22) and (A23) attached to the $\mathcal{P}_3$ transformation, a partner $\mathcal{P}_3 \Phi^I_{MNn'}$ of $\mathcal{P}_3 \Phi^I_{MNn}$ can always be found provided that $n' = n+2$, or $n+4$, or $n+6$. The lower possible n' value is actually adopted, which fixes $\sigma^I_{Nnn'}$. Of course, the linear combination (A31) is formed only if both $\mathcal{A}^{IM}_{\mu mNn}$ and $\mathcal{A}^{IM}_{\mu mNn'}$ belong to the basis set labeled INIT previously.

This discussion was introduced to cure a specific pathology. When no pathology exists, that is, for the special case where the $K \neq 0$ and $K/2$ even components $\mathcal{P}_3 \Phi^I_{MNn}$ vanish (i.e., for $C^I_{NKn} = 0$) and obviously for components in the $I < 4$ spin blocks, we also adopt the notation $\Gamma^{IM}_{\mu mNn}$ for the basis state $\mathcal{A}^{IM}_{\mu mNn}$.

As a by-product of using the ''paired'' basis states $\Gamma^{IM}_{\mu mNn}$ (A32) in a given subspace of angular momentum, the number N_Γ of functions fulfilling the boundary conditions and built from the original N^{INIT}_I functions $\mathcal{A}^{IM}_{\mu mNn}$, has the property: $N_\Gamma \leqslant N^{INIT}_I$. The numbers of basis states thus obtained are identified by the label BOUND in Fig. 22. As can be seen, the effect of including boundary conditions is a reduction of the number of basis functions with $I \geqslant 4$. This reduction gets stronger as I increases, and reaches typically 15 % for $I = 22$.

3. Numerical methods

The physical states $\Psi_{IM\alpha}$ (40) now defined in terms of the basis functions $\Gamma^{IM}_{\mu mNn}$ are written

$$\Psi_{IM\alpha}(\beta,\gamma,\Omega) = \sum_{\mu=1}^{\mu_{max}} \sum_{n=0,1,2\ldots}^{m_{\max''}} \sum_{m=n,n+2,\ldots}^{m_{\max''}} \times \sum_N^{N_{\max'}} T^{I\alpha}_{\mu mNn} \Gamma^{IM}_{\mu mNn}(\beta,\gamma,\Omega), \tag{A33}$$

where the $T^{I\alpha}_{\mu mNn}$'s are coefficients attached to this expansion, and where the summation notation Σ' has the same meaning as before. A new symbol Σ'' is introduced. This short notation means that the summation is restricted to the basis functions $\Gamma^{IM}_{\mu mNn}$ which were not excluded previously.

a. Truncations

The configuration space spanned by the basis functions Γ is truncated as follows. First, consider the number $\mu_{\max}$ of

exponential weight functions Q_μ. Since we treat on the same grounds ND and SD collective levels, we adopt the value $\mu_{\max}=2$. We have checked that this prescription generates a set of basis vectors which is rich enough to secure the stability of our predictions.

Next, consider the index m. This number is characteristic of (i) the order of the power expansion (A21) and (ii) the number of nodes (A19) in the Fourier components (A18). The maximum value adopted for m is $m_{\max}=36$. We have shown earlier in Fig. 22 that this value is large enough to secure the stability in energy of the predicted collective levels. This specific truncation is relevant to the vibration amplitudes expanded in terms of the coordinates β and γ. When expanding the amplitudes now expressed in the Cartesian coordinates a_0 and a_2, components of the form $(a_0)^i(a_2)^j$ are obtained. These two separate expansions of the vibration amplitudes are equivalent provided that $(i+j)\leqslant m_{\max}$.

Now consider the number N which bears similarities with K, the projection of angular momentum on the symmetry axis. The N values exclusively depend upon the values taken by the number $\mathcal{N}_n^I$ of linearly independent $P_3\Phi_{MNn}^I$ functions. In the range $0\leqslant I\leqslant 22$, $\mathcal{N}_n^I$ takes on values from 0 to 4 (see Fig. 21). Here, the truncation $(\mathcal{N}_n^I)_{\max}=2$ is adopted (and marked by the shaded area in Fig. 21). This implies that the basis states with $\{N=4$ or 6, $I=$even$\}$ and with $\{N=6$ or 8, $I=$odd$\}$ indexes are removed from the summation over N in Eq. (A33), which fixes $N_{\max}$. The total numbers N_I of state vectors in the block of spin I, calculated in the range $I=0$–22, are shown in Fig. 22 where the label TRUNC means that $\mathcal{N}_n^I\leqslant 2$. As can be seen, the truncation alters the N_I values determined for $I\geqslant 12$ and leaves unchanged N_I for $I<12$. Although impressive at high spin, this reduction leaves over complete our vector basis.

The truncation $\mathcal{N}_n^I\leqslant 2$ implies that some levels with $I\geqslant 12$ are ignored. We have checked in the SD region that no discontinuities show up when comparing the excitation energies predicted for the yrast, β, and γ bands at spins higher and lower than $I=12$. This is the strongest argument to support this geometric truncation. Moreover, adopting $\mathcal{N}_n^I\leqslant 2$ in our analyses enhances the relative weight of small K components in the predicted wave functions because δ_{KN} is the leading-order term in the geometric factors C_{NKn}^I (A23). We therefore consider that $\mathcal{N}_n^I\leqslant 2$ is a reliable approximation for $I\geqslant 12$ because we are dealing only with the first SD bands which all are strongly dominated by low-K components. The truncation $\mathcal{N}_n^I\leqslant 2$ may just alter the spectra predicted at high excitation energies.

b. Matrix elements

In the representation (A33), we need to calculate the Hamiltonian kernel

$$\mathcal{H}_{cc'}=\langle\Gamma_c^I|\hat{\mathcal{H}}_{\rm coll}|\Gamma_{c'}^I\rangle \tag{A34}$$

and the overlap kernel

$$\mathcal{O}_{cc'}=\langle\Gamma_c^I|\Gamma_{c'}^I\rangle, \tag{A35}$$

where c is the channel $\{\mu,\ m,\ N,\ n\}$. In the (β,γ) collective coordinates, these kernels are written

$$\mathcal{H}_{cc'}=\int d\Omega\int_S(\Gamma_c^I\hat{\mathcal{H}}_{coll}\Gamma_{c'}^I)^{1/2}\beta d\beta d\gamma \tag{A36}$$

and

$$\mathcal{O}_{cc'}=\int d\Omega\int_S(\Gamma_c^I\Gamma_{c'}^I)[D(\beta,\gamma)]^{1/2}\beta d\beta d\gamma, \tag{A37}$$

respectively. These kernels are calculated over the sextant $S=\{\beta\geqslant 0,0\leqslant\gamma\leqslant\pi/3\}$ using the mesh $(\Delta\beta,\Delta\gamma)=(1/70,\pi/180)$. Furthermore, the maximum value $\beta_{\max}$ is of the order of 0.92. Precise cutoff values are not given because the actual $\beta_{\max}$'s are fixed for each nucleus using the criteria that the magnitude of the exponential weights Q_μ should be lower than 10^{-7} at far edge. Finally, integration over the domain is performed for both $\mathcal{H}_{cc'}$ and $\mathcal{O}_{cc'}$ with approximately 4000 points. Integration over the Euler angles, on the other hand, is straightforward because the Γ_c^I and $\mathcal{H}_{\rm coll}\Gamma_c^I$ functions are always expressed in terms of Wigner matrices.

c. Orthonormalization

Next, we proceed to the orthonormalization of the basis set using the well-known Gramm-Schmidt method. The excluded basis states have norms weaker than 2×10^{-4}, and the absolute values of nondiagonal $\mathcal{O}_{cc'}$ matrix elements are always lower than 2×10^{-7} in the new basis. The N_I values thus obtained for ^{192}Hg are shown at the right hand side of Fig. 22 where the notation ORTHO is used. Approximately 60% of the original of basis states in each spin block are rejected. For instance, the $I=0$ subspace now is spanned by $N_{(I=0)}=98$ orthonormalized basis states and that for $I=22$ involves only $N_{(I=22)}=390$ vectors. Similar results are obtained for the other nuclei. These dimensions are numerically tractable. Solving $\hat{\mathcal{H}}_{\rm coll}$ now reduces to a simple eigenvalue problem which is treated through standard matrix diagonalization.

d. Optimum basis sets

The content of basis states and the number $N_I^{\rm ORTHO}$ in Fig. 22 depend upon the selected parameters $\alpha_{l\mu}$ in Eq. (A26). All the $N_I^{\rm ORTHO}$'s used when solving $\hat{\mathcal{H}}_{\rm coll}$ are determined after the basis parameters have been optimized. This optimization method is described below.

The free parameters are embedded in the exponential weights Q_μ defined in Eq. (A26). They are optimized in such a way that the first 0^+ levels predicted at normal and superdeformed shapes take on energies as low as possible. For the ground state, this method is nothing but the application of the variational principle. This variational principle might be adopted in the region of superdeformation as long as the 0^+ SD level component at normal deformation is weak. We have adopted this view and tested its reliability through checking the stability of our predictions upon increasing the basis size. This size is governed by the parameter $m_{\max}$ (A21) which is increased from a starting value m_{st}.

In the numerical optimization process which is repeated for each nucleus, we fix $m_{\max}$ to $m_{\max}=m_{st}=20$. In the first step, the parameter sets (α_{l1}) and (α_{l2}) in Q_1 and Q_2, respectively, are guessed separately through solving $\hat{\mathcal{H}}_{\rm coll}$ with one-center bases. The parameter sets $(\alpha_{l1})^{(1)}$ and $(\alpha_{l2})^{(1)}$ thus obtained are used in calculations involving the two-center basis. In step 2, the parameter set attached to Q_1 is optimized to minimize the ground state energy. A new set $(\alpha_{l1})^{(2)}$ is obtained. In step 3, $(\alpha_{l1})^{(2)}$ is used in a new two-center basis calculation to minimize the energy of the first 0^+ state exhibiting SD character. A new set $(\alpha_{l2})^{(2)}$ is obtained. This iterative method is repeated over and over from step 2 until stability of the predictions at normal and superdeformed shapes is reached. The last step consists in solving $\hat{\mathcal{H}}_{\rm coll}$ for spins $I>0$. Then $m_{\max}$ is increased until stability of all level predictions is obtained. As shown in Fig. 4, stability occurs for $m_{\max}=36$. This value is common to all calculations performed in the $A\sim 190$ region.

[1] S. M. Polikanov *et al.*, Sov. Phys. JETP **15**, 1016 (1962).
[2] V. M. Strutinsky, Nucl. Phys. **A95**, 420 (1967); **A122**, 1 (1968).
[3] C. F. Tsang and S. G. Nilsson, Nucl. Phys. **A140**, 275 (1970).
[4] U. Götz, H. C. Pauli, K. Adler, and K. Junker, Nucl. Phys. **A192**, 1 (1972).
[5] I. Ragnarsson and R. K. Sheline, Phys. Scr. **29**, 385 (1984).
[6] M. Girod, J.-P. Delaroche, and J.-F. Berger, Phys. Rev. C **38**, 1519 (1988).
[7] S. Frauendorf and F. R. May, Phys. Lett. **125B**, 245 (1983).
[8] W. Nazarewicz *et al.*, Nucl. Phys. **A435**, 397 (1985).
[9] S. Frauendorf and R. Bengtsson, Nucl. Phys. **A327**, 139 (1979).
[10] I. Ragnarsson *et al.*, Nucl. Phys. **A347**, 287 (1980).
[11] J. Dudek and W. Nazarewicz, Phys. Rev. C **31**, 298 (1985); J. Dudek, W. Nazarewicz, Z. Szytmanski, and G. A. Leander, Phys. Rev. Lett. **59**, 1405 (1987); J. Dudek, T. Werner, and L. L. Riedinger, Phys. Lett. B **211**, 252 (1988).
[12] T. Bengtsson, S. Åberg, and I. Ragnarsson, Phys. Lett. B **208**, 39 (1988).
[13] R. R. Chasman, Phys. Lett. B **219**, 227 (1989); **242**, 317 (1990).
[14] W. Nazarewicz, R. Wyss, and A. Johnson, Nucl. Phys. **A503**, 285 (1989).
[15] M. A. Riley *et al.*, Nucl. Phys. **A512**, 178 (1990).
[16] W. Satula, S. Cwiok, W. Nazarewicz, R. Wyss, and A. Johnson, Nucl. Phys. **A529**, 289 (1991).
[17] T. Nakatsukasa, K. Matsuyanagi, S. Mizutori, and Y. R. Shimizu, Phys. Rev. C **53**, 2213 (1996); T. Nakatsukasa, Acta Phys. Pol. B **27**, 59 (1996).
[18] P. J. Twin *et al.*, Phys. Rev. Lett. **57**, 811 (1986).
[19] Xiao-Ling Han and Cheng-Li Wu, At. Data Nucl. Data Tables **63**, 117 (1996), and references therein.
[20] J. F. Sharpey-Schafer and J. Simpson, Prog. Part. Nucl. Phys. **21**, 293 (1988).
[21] S. Åberg, H. Flocard, and W. Nazarewicz, Annu. Rev. Nucl. Part. Sci. **40**, 439 (1990).
[22] R. V. F. Janssens and T. L. Khoo, Annu. Rev. Nucl. Part. Sci. **41**, 321 (1991).
[23] M. Meyer and J. P. Vivien, Ann. Phys. (Paris) **17**, 11 (1992).
[24] C. Backtash, B. Haas, and W. Nazarewicz, Annu. Rev. Nucl. Part. Sci. **45**, 485 (1995).
[25] A. Lopez-Martens *et al.*, Phys. Lett. B **380**, 18 (1996).
[26] T. H. R. Skyrme, Nucl. Phys. **9**, 15 (1959).
[27] D. Vautherin and D. M. Brink, Phys. Rev. C **5**, 626 (1972).
[28] M. Beiner, H. Flocard, N. Van Giai, and Quentin, Nucl. Phys. **A238**, 29 (1975).
[29] J. Bartel, P. Quentin, M. Brack, C. Guet, and H. B. Håkansson, Nucl. Phys. **A386**, 79 (1982).
[30] E. Chabanat, P. Bonche, P. Haensel, J. Meyer, and R. Schaeffer, Nucl. Phys. **A627**, 710 (1997).
[31] D. Gogny, in *Proceedings of the International Conference on Nuclear Physics*, Munich, 1973, edited by J. De Boer and H. J. Mang (North Holland, Amsterdam, 1973); in *Proceedings of the International Conference on Nuclear Selfconsistent Fields*, Trieste, 1975, edited by G. Ripka and M. Porneuf (North Holland, Amsterdam, 1975).
[32] J. Dechargé and D. Gogny, Phys. Rev. C **21**, 1568 (1980).
[33] J.-F. Berger, M. Girod, and G. Gogny, Comput. Phys. Commun. **63**, 365 (1991).
[34] P. Ring, Prog. Part. Nucl. Phys. **37**, 193 (1996).
[35] T. Gonzalez-Llarena, J. L. Egido, G. A. Lalazissis, and P. Ring, Phys. Lett. B **379**, 13 (1996).
[36] M. Cailliau, J. Letessier, H. Flocard, and P. Quentin, Phys. Lett. **46B**, 11 (1973).
[37] M. Girod, J.-P. Delaroche, D. Gogny, and J.-F. Berger, Phys. Rev. Lett. **62**, 2452 (1989).
[38] P. Bonche, S. J. Krieger, P. Quentin, M. S. Weiss, J. Meyer, M. Meyer, N. Redon, H Flocard;, and P.-H. Heenen, Nucl. Phys. **A500**, 308 (1989).
[39] M. Meyer, N. Redon, P. Quentin, and J. Libert, Phys. Rev. C **45**, 233 (1992).
[40] S. K. Patra, S. Yoshida, N. Takigawa, and C. R. Praharaj, Phys. Rev. C **50**, 1924 (1994).
[41] S. Takahara, N. Tajima, and N. Onishi, Nucl. Phys. **A642**, 461 (1998).
[42] P. Bonche, J. Dobaczewski, H. Flocard, P.-H. Heenen, and J. Meyer, Nucl. Phys. **A510**, 466 (1990); P. Bonche, J. Dobaczewski, H. Flocard, P.-H. Heenen, J. Meyer, and M. S. Weiss, *ibid.* **A519**, 509 (1990).
[43] J. Skalski, P.-H. Heenen, P. Bonche, H. Flocard, and J. Meyer, Nucl. Phys. **A551**, 109 (1993).
[44] S. J. Krieger, P. Bonche, H. Flocard, P. H. Heenen, R. Mehrem, and M. S. Weiss, Phys. Rev. C **54**, 2399 (1996).
[45] J.-P. Delaroche *et al.*, Phys. Rev. C **50**, 2332 (1994).
[46] J.-P. Delaroche, M. Girod, J. Libert, and I. Deloncle, Phys. Lett. B **232**, 145 (1989).
[47] M. Girod, J. P. Delaroche, J. Libert, and I. Deloncle, Phys. Rev. C **45**, R1420 (1992).
[48] B. Gall, P. Bonche, J. Dobaczewski, H. Flocard, and P.-H.

Heenen, Z. Phys. A **348**, 183 (1994).
[49] J. Terasaki, P.-H. Heenen, P. Bonche, J. Dobaczewski, and H. Flocard, Nucl. Phys. **A593**, 1 (1995).
[50] P.-H. Heenen and R. V. F. Janssens, Phys. Rev. C **57**, 159 (1998).
[51] M. Girod, J.-P. Delaroche, J.-F. Berger, and J. Libert, Phys. Lett. B **325**, 1 (1994).
[52] M. Girod, J.-P. Delaroche, J.-F. Berger, S. Peru, and J. Libert, Z. Phys. A **358**, 177 (1997).
[53] A. Valor, J. L. Egido, and L. M. Robledo, Phys. Lett. B **393**, 249 (1997).
[54] A. V. Afanasjev, J. König, and P. Ring, Nucl. Phys. **A608**, 107 (1996).
[55] D. R. Inglis, Phys. Rev. **103**, 1786 (1956).
[56] S. T. Belyaev, Nucl. Phys. **24**, 322 (1961).
[57] D. J. Thouless and J. G. Valatin, Nucl. Phys. **31**, 211 (1962).
[58] D. L. Hill and J. A. Wheeler, Phys. Rev. **89**, 1102 (1953); J. J. Griffin and J. A. Wheeler, *ibid.* **108**, 311 (1957).
[59] M. Girod and B. Grammaticos, Nucl. Phys. **A330**, 40 (1979).
[60] D. H. Schiff and B. Jancovici, Nucl. Phys. **58**, 678 (1964).
[61] A. Kamlah, Z. Phys. **216**, 52 (1968).
[62] F. M. H. Villars, in *Proceedings of the International Conference on Nuclear Selfconsistent Fields*, Trieste, 1975, edited by G. Ripka and M. Porneuf (North Holland, Amsterdam, 1975).
[63] K. Kumar and M. Baranger, Nucl. Phys. **A92**, 608 (1967).
[64] M. Baranger and M. Véneroni, Ann. Phys. (N.Y.) **114**, 123 (1978).
[65] F. M. H. Villars, Nucl. Phys. **A285**, 269 (1977).
[66] K. Goeke and P. G. Reinhard, Ann. Phys. (N.Y.) **124**, 249 (1980).
[67] M. Girod and B. Grammaticos, Phys. Rev. C **27**, 2317 (1983).
[68] E. Yuldashbaeva, J. Libert, P. Quentin, and M. Girod, Report No. CENBG 98-33, Phys. Lett. B (to be published).
[69] P. Ring and P. Schuck, *The Nuclear Many-Body Problem* (Springer, Berlin, 1980), p. 471.
[70] E. Iouldachbaeva, Ph.D. thesis, Univ. Bordeaux I, 1997.
[71] M.-J. Giannoni and P. Quentin, Phys. Rev. C **21**, 2060 (1980); **21**, 2076 (1980).
[72] L. Bennour. Ph.D. thesis, Univ. Paris-Sud Orsay, 1987.
[73] A. Bohr, K. Dan. Vidensk. Selsk. Mat. Fys. Medd. **26**, 14 (1952).
[74] J. W. Negele and G. Rinker, Phys. Rev. C **15**, 1499 (1977).
[75] T. L. Khoo *et al.*, Phys. Rev. Lett. **76**, 1583 (1996).
[76] D. P. McNabb *et al.*, Phys. Rev. C **56**, 2474 (1997).
[77] M. J. Brinkman *et al.*, Phys. Rev. C **53**, 1461 (1996); K. Hauschild *et al.*, *ibid.* **55**, 2819 (1997).
[78] S. Åberg, Phys. Rev. Lett. **82**, 299 (1999).
[79] T. Lauritsen *et al.*, Phys. Rev. Lett. **69**, 2479 (1992).
[80] R. G. Henry *et al.*, Phys. Rev. Lett. **73**, 777 (1994).
[81] A. Lopez-Martens, Ph.D. thesis, Univ. Paris-Sud Orsay, 1996.
[82] T. L. Khoo *et al.*, Nucl. Phys. **A557**, 83c (1993).
[83] V. Metag, D. Habbs, and H.-J. Specht, Phys. Rep. **65**, 1 (1980).
[84] H. A. Weidenmüller, P. Von Brentano, and B. R. Barrett, Phys. Rev. Lett. **81**, 3603 (1998).
[85] I. Ragnarsson and S. Åberg, Phys. Lett. B **180**, 191 (1986); E. Vigezzi, R. A. Broglia, and T. Døssing, *ibid.* **249**, 163 (1990); Y. R. Shimizu *et al.*, *ibid.* **274**, 253 (1992); Y. R. Shimizu *et al.*. Nucl. Phys. **A557**, 99c (1993).
[86] R. Krücken *et al.*, Phys. Rev. Lett. **73**, 3359 (1994).
[87] M. W. Drigert *et al.*, Nucl. Phys. **A530**, 452 (1991); H. Amro *et al.*, Phys. Lett. B **413**, 15 (1997).
[88] P. Willsau *et al.*, Nucl. Phys. **A574**, 560 (1994); E. F. Mooore *et al.*, Phys. Rev. C **55**, R2150 (1997); B. C. Busse *et al.*, *ibid.* **57**, R1017 (1998).
[89] J. R. Hughes *et al.*, Phys. Rev. Lett. **72**, 824 (1994); R. Kühn *et al.*, Phys. Rev. C **55**, R1002 (1997); E. F. Moore *et al.*, *ibid.* **55**, R2150 (1997).
[90] P. Willsau *et al.*, Z. Phys. A **344**, 351 (1993); R. Krücken *et al.*, Phys. Rev. C **55**, R1625 (1997).
[91] E. F. Moore *et al.*, Phys. Rev. C **48**, 2261 (1993).
[92] G. Hackman *et al.*, Phys. Rev. Lett. **79**, 4100 (1997).
[93] U. Goerlach, D. Habbs, V. Metag, B. Schwartz, H. J. Specht, and H. Backe, Phys. Rev. Lett. **48**, 1160 (1982).
[94] H. Dancer, S. Perriès, P. Bonche, H. Flocard, P.-H. Heenen, and J. Meyer, in Proceedings of the International Nuclear Physics Conference, Paris, 1998, Nucl. Phys. A (to be published).
[95] D. Brink and G.R. Satchler, *Angular Momentum* (Claredon, Oxford, 1962), p. 21.
[96] J. Libert and P. Quentin, Z. Phys. A **306**, 315 (1982).